



Since January 2020 Elsevier has created a COVID-19 resource centre with free information in English and Mandarin on the novel coronavirus COVID-19. The COVID-19 resource centre is hosted on Elsevier Connect, the company's public news and information website.

Elsevier hereby grants permission to make all its COVID-19-related research that is available on the COVID-19 resource centre - including this research content - immediately available in PubMed Central and other publicly funded repositories, such as the WHO COVID database with rights for unrestricted research re-use and analyses in any form or by any means with acknowledgement of the original source. These permissions are granted for free by Elsevier for as long as the COVID-19 resource centre remains active.



ORIGINAL ARTICLE

# Synthesis of indole-based oxadiazoles and their interaction with bacterial peptidoglycan and SARS-CoV-2 main protease: In vitro, molecular docking and in silico ADME/Tox study



Mohammad Azam Ansari<sup>a,\*</sup>, Muhammad Taha<sup>b,\*</sup>, Nizam Uddin<sup>c</sup>, Fazal Rahim<sup>d</sup>, Qazi Mohammad Sajid Jamal<sup>e</sup>, Mohammad N. Alomary<sup>f</sup>, Fahad M. Alshabrmi<sup>g</sup>, Ahmad Almatroudi<sup>g</sup>, Banan Atwah<sup>h</sup>, Zain Alhindi<sup>h</sup>, Naveed Iqbal<sup>i</sup>, Khalid Mohammed Khan<sup>j</sup>

<sup>a</sup> Department of Epidemic Disease Research, Institute for Research and Medical Consultations (IRMC), Imam Abdulrahman Bin Faisal University, Dammam 31441, Saudi Arabia

<sup>b</sup> Department of Clinical Pharmacy, Institute for Research and Medical Consultations (IRMC), Imam Abdulrahman Bin Faisal University, Dammam 31441, Saudi Arabia

<sup>c</sup> Department of Chemistry, University of Karachi, Karachi 75270, Pakistan

<sup>d</sup> Department of Chemistry, Hazara University, Mansehra-21300, Khyber Pakhtunkhwa, Pakistan

<sup>e</sup> Department of Health Informatics, College of Public Health and Health Informatics, Qassim University, Al Bukayriyah, Saudi Arabia

<sup>f</sup> National Centre for Biotechnology, King Abdulaziz City for Science and Technology (KACST), Riyadh 11442, Saudi Arabia

<sup>g</sup> Department of Medical Laboratories, College of Applied Medical Sciences, Qassim University, Qassim 51452, Saudi Arabia

<sup>h</sup> Laboratory Medicine Department, Faculty of Applied Medical Sciences, Umm Al-Qura University, Makkah, Saudi Arabia

<sup>i</sup> Department of Chemistry, University of Poonch, Rawalakot, AJK, Pakistan

<sup>j</sup> H. E. J. Research Institute of Chemistry, International Center for Chemical and Biological Sciences, University of Karachi, Karachi 75270, Pakistan

Received 24 February 2022; revised 31 March 2022; accepted 31 March 2022

Available online 9 April 2022

## KEYWORDS

Indole;  
Oxadiazole;

**Abstract** In the present study, Indole-based-oxadiazole (1A-17A) compounds were successfully synthesized. The structures of all synthesized compounds were fully characterized by different sophisticated spectroscopic techniques such as <sup>1</sup>H NMR, <sup>13</sup>C NMR, and HREI-MS. Further, the

\* Corresponding authors.

E-mail addresses: [maansari@iau.edu.sa](mailto:maansari@iau.edu.sa) (M.A. Ansari), [mtaha@iau.edu.sa](mailto:mtaha@iau.edu.sa) (M. Taha).

Peer review under responsibility of King Saud University.



Main protease;  
Peptidoglycan;  
Multidrug resistant;  
Antibiofilm;  
SARS-CoV2

synthesized compounds were explored to investigate their broad-spectrum antibacterial and anti-biofilm potential against multidrug resistant *Pseudomonas aeruginosa* (MDR-PA) and methicillin resistant *Staphylococcus aureus* (MRSA). The compounds possessed a broad spectrum of antibacterial activity having MIC values of values 1–8 mg/ml against the tested microorganisms. Compound A6 and A7 shows maximum antibacterial activity against MDR-PA, whereas A6, A7 and A11 shows highest activity against MRSA. Furthermore, antibiofilm assay shows that A6, A7 and A11 showed maximum inhibition of biofilm formation and it was found that at 4 mg/ml; A6, A7 and A11 inhibit MRSA biofilm formation by 81.1, 77.5 and 75.9%, respectively; whereas in case of *P. aeruginosa*; A6 and A7 showed maximum biofilm inhibition and inhibit biofilm formation by 81.5 and 73.7%, respectively. Molecular docking study showed that compounds A6, A7, A8, A10, and A11 had high binding affinity to bacterial peptidoglycan, indicating their potential inhibitory activity against tested bacteria, whereas A6 and A11 were found to be the most effective inhibitors of SARS CoV-2 main protease (3CLpro), with a binding affinity of  $-7.78$  kcal/mol. Furthermore, SwissADME and pkCSM-pharmacokinetics online tools was applied to calculate the ADME/Tox profile of the synthesized compounds and the toxicity of these chemicals was found to be low. The Lipinski, Veber, Ghose, and Consensus LogP criteria were also used to predict drug-likeness levels of the compounds. Our findings imply that the synthesized compounds could be a useful for the preventing and treating biofilm-related microbial infection as well as SARS-CoV2 infections.

© 2022 The Authors. Published by Elsevier B.V. on behalf of King Saud University. This is an open access article under the CC BY-NC-ND license (<http://creativecommons.org/licenses/by-nc-nd/4.0/>).

## 1. Introduction

The emergence and re-emergence of antimicrobial drug resistance due to their inappropriate and excessive use by a large number of disease-causing bacterial strains not only pose a great threat to the community health but also pose a challenge for the researchers to design and developed new antimicrobial drug [1]. Regardless of presence of antibacterial therapy, the rate of disease and death associated with bacterial infections remain increasing, because of their ability to develop resistance to most of the present antibiotics [2]. The infections caused by biofilm producing multidrug resistant bacterial strains such as *Staphylococcus aureus* and *Pseudomonas aeruginosa* are also a major threat because biofilm matrix obstructs the penetration of antibiotics inside the biofilm matrix [3]. On the other hand, in December 2019 in Wuhan, China, a newly deadly emerged coronavirus strain (COVID-19) has infected nearly the whole world's population that has produced an immediate urgency to discover promising targets for the treatment of COVID-19. As of February 2, 2022, 382,556,840 confirmed COVID-19 cases and 5,707,556 COVID-19-related deaths have been reported across the globe (<https://www.worldometers.info/coronavirus/>[4]). In response to the COVID-19 pandemic, researchers have made significant progress in developing potential medical therapies. Several compounds are now being evaluated for their efficacy against COVID-19 illness, with some having progressed to clinical trials and others still in the preclinical phase [5]. The nitrogen-containing heterocyclic compounds are reported to have far better activities [6,7,8,9,10,11] than any other heteroatom compounds. Indole is the bicyclic compound having nitrogen in five-member ring. Indole heterocycle is broadly spread in nature. The tryptophan and serotonin are found in numerous natural alkaloids which have indole ring as basic structure. Indole compounds reported to retain numerous biological and pharmacological activities and consequently have energized medicinal chemists for discovering them for additional research [12]. Indole analogues

displayed a large range of biological behaviors including anti-cancer [13], antimicrobial [14], anti-inflammatory [15], anti-malarial [16], anti-tubercular [17], as anti-diabetic agents [18],  $\beta$ -glucuronidase, [19], and urease inhibition [20] activities. While some natural alkaloids having indole also showed biological potential [21]. Fluorine substituted compounds reported to have great industrial attraction in the past years [22,23]. Effective synthetic methods established to spot fluorine on a heterocyclic ring while the manufacturing of fluorine containing compounds to target for possible therapeutic uses [24,25]. The binding affinity and structure of protein-drug complexes are critical for deciphering the molecular mechanism involved in drug development. Additionally, the SARS-CoV-2 main protease (PDB ID: 6LU7) and bacterial peptidoglycan (PDB ID: 2MTZ) are key target for the development of anti- COVID-19 and antibacterial drugs. Moreover, the development of new antiviral or antibacterial drugs is not an easy task, as it required intensive time, labors and funds. Consequently, an alternative and non-traditional strategies are desirable to identify and develop new class of compounds that only not control infections but also overcome antibiotics resistance developed by a variety of pathogenic bacteria and viruses. Therefore, the designing and development of new class of broad-spectrum antimicrobial and antiviral compounds with reduced toxicity and higher specificity is of great interest for the academicians, researchers and pharmaceutical industries. The objective of present study was (i) synthesis of indole-based-oxadiazole (1A-17A) compounds, (ii) Characterization of synthesized compounds by different sophisticated spectroscopic techniques such 1H NMR, 13C NMR and HREI-MS, (iii) investigation of their broad-spectrum antibacterial activity against gram-negative MDR-PA and gram-positive MRSA bacterial strains, (iv) investigation of antibiofilm potential of synthesized compounds against MDR-PA and MRSA, (v) interaction of top ranked compounds with bacterial peptidoglycan (PDB ID: 2MTZ) using molecular docking analysis, and (vi) molecular docking and in silico ADME/Tox profile

analysis of the synthesized compounds with SARS CoV-2 main protease (3CLpro).

## 2. Material and methods

### 2.1. General experiment

The <sup>1</sup>H NMR and <sup>13</sup>C NMR experiments were carried out using an Avance Bruker 300 MHz. HR-MS was determined in positive/negative mode on an Agilent 6330 Ion Trap. The Perkinelmer instrument was used to do the element analysis. Stuart (SMP-10) melting point device was used to record the melting point. Thin layer chromatography (TLC) was carried out using pre-coated silica gel aluminum foils (Germany). Chromatograms at 254 and 365 nm were seen using a UV light.

### 2.2. Synthesis of 5-fluoroindoline-3-carbohydrazide

The 5-fluoroindoline-2-carbohydrazide was made by combining 25 mmol methyl 5-fluoro-1H-indole-2-carboxylate with 10 mL hydrazine hydrate in 50 mL methanol for 6 h. The solvent was evaporated once the reaction was completed, and the crude product was washed with cold water before being recrystallized in methanol.

### 2.3. General procedure for the synthesis of compounds (1–17)

In POCl<sub>3</sub> (10 mL), a combination of 5-fluoro-1H-indole-2-carbohydrazide (0.3 mmol) and various (1–17) aromatic acids (0.33 mmol) was refluxed for 4–6 h. The mixture was allowed to cool before being added to cold water. To eliminate the HCl created during the reaction, the mixture was reacted with NaHCO<sub>3</sub>. The ppt formed was filtered, dried, and crystallized in methanolic solution.

#### 2.3.1. 2-(4-bromophenyl)-5-(5-fluoro-1H-indol-2-yl)-1,3,4-oxadiazole (1)

Yield: (83%); <sup>1</sup>HNMR (300 MHz, DMSO *d*<sub>6</sub>): δ 12.52 (s, NH, 1H), 7.56 (d, *J* = 8.2 Hz, 1H), 7.52–7.47 (m, 4H), 7.26 (s, 1H), 7.12 (d, *J* = 8.6 Hz); <sup>13</sup>CNMR (75 MHz, DMSO *d*<sub>6</sub>) δ 164.0 (C), 163.6 (C), 150.2 (d, *J* = 175, C-F), 132.5 (C), 131.6 (CH), 131.6 (CH), 129.4 (C), 129.3 (CH), 129.3 (CH), 124.8 (C), 124.2 (C), 122.5 (C), 115.0 (CH), 110.0 (CH), 109.5 (CH), 100.4 (CH); HREI-MS: *m/z* calcd for C<sub>16</sub>H<sub>9</sub>BrFN<sub>3</sub>O, [M]<sup>+</sup> 356.9913; Found: 356.9950.

#### 2.3.2. 2-(5-fluoro-1H-indol-2-yl)-5-(2-fluorophenyl)-1,3,4-oxadiazole (2)

Yield: (82%); <sup>1</sup>HNMR (300 MHz, DMSO *d*<sub>6</sub>): δ 12.46 (s, NH, 1H), 7.49 (t, *J* = 7.1 Hz, 1H), 7.41–7.22 (m, 6H), 7.06 (t, *J* = 6.2 Hz, 1H); <sup>13</sup>CNMR (75 MHz, DMSO *d*<sub>6</sub>) δ 164.0 (C), 163.6 (C), 123.8 (C), 158.0 (d, *J* = 182, C-F), 150.1 (d, *J* = 172, C-F), 132.5 (C), 130.5 (C), 129.4 (C), 129.3 (C), 124.6 (C), 124.2 (C), 115.3 (CH), 114.5 (C), 110.0 (CH), 109.5 (CH), 100.4 (CH); HREI-MS: *m/z* calcd for C<sub>16</sub>H<sub>9</sub>F<sub>2</sub>N<sub>3</sub>O, [M]<sup>+</sup> 297.0714; Found: 297.0749.

#### 2.3.3. 2-(5-fluoro-1H-indol-2-yl)-5-(4-nitrophenyl)-1,3,4-oxadiazole (3)

Yield: (86%); <sup>1</sup>HNMR (300 MHz, DMSO *d*<sub>6</sub>): δ 12.63 (s, 1H, NH), 8.34 (d, 2H, *J* = 8.1 Hz), 8.15 (d, 2H, *J* = 8.1 Hz), 7.38 (m, 2H), 7.22 (d, 1H, *J* = 7.1 Hz), 6.98–6.94 (m, 1H); <sup>13</sup>CNMR (75 MHz, DMSO *d*<sub>6</sub>) δ 164.0 (C), 163.5 (C), 150.2 (d, *J* = 175, C-F), 147.5 (C) 132.5 (C), 132.0 (C), 131.5 (CH), 131.5 (CH), 129.4 (C), 129.1 (CH), 129.1 (CH), 124.2 (C), 115.0 (CH), 110.0 (CH), 109.5 (CH), 100.4 (CH); HREI-MS: *m/z* calcd for C<sub>16</sub>H<sub>9</sub>FN<sub>4</sub>O<sub>3</sub>, [M]<sup>+</sup> 324.0659; Found: 324.0611.

#### 2.3.4. 2-(5-fluoro-1H-indol-2-yl)-5-(4-isopropylphenyl)-1,3,4-oxadiazole (4)

Yield: (81%); <sup>1</sup>HNMR (300 MHz, DMSO *d*<sub>6</sub>): δ 11.64 (s, 1H, NH), 8.27 (d, 2H, *J* = 7.4 Hz), 8.01 (d, 2H, *J* = 7.3 Hz), 7.71–7.63 (m, 2H), 7.14 (s, 1H), 7.01–6.95 (m, 1H), 3.41 (m, 1H, CH), 2.42 (s, 6H, 2xCH<sub>3</sub>); <sup>13</sup>CNMR (75 MHz, DMSO *d*<sub>6</sub>) δ 164.0 (C), 164.2 (C), 150.4 (d, *J* = 178, C-F), 148.0 (C), 142.0 (C), 132.5 (C), 129.4 (C), 129.0 (CH), 129.0 (CH), 127.5 (CH), 127.5 (CH), 124.5 (C), 115.0 (CH), 110.0 (CH), 109.5 (CH), 100.4 (CH), 33.0 (–CH<sub>2</sub>), 23.0 (CH<sub>3</sub>), 23.0 (CH<sub>3</sub>); HREI-MS: *m/z* calcd for C<sub>16</sub>H<sub>14</sub>FN<sub>3</sub>O<sub>4</sub>S, [M]<sup>+</sup> 363.0689; Found: 363.0688. HREI-MS: *m/z* calcd for C<sub>19</sub>H<sub>16</sub>FN<sub>3</sub>O, [M]<sup>+</sup> 321.1277; Found: 321.1235.

#### 2.3.5. 2-(5-fluoro-1H-indol-2-yl)-5-(*p*-tolyl)-1,3,4-oxadiazole (5)

Yield: (83%); <sup>1</sup>HNMR (300 MHz, DMSO *d*<sub>6</sub>): δ 12.66 (s, NH, 1H), 8.11 (d, *J* = 8.2 Hz, 2H), 7.70–7.63 (m, 2H), 7.22 (d, *J* = 8.2 Hz, 2H), 7.03–6.94 (m, 2H), 2.36 (s, 3H, CH<sub>3</sub>); <sup>13</sup>CNMR (75 MHz, DMSO *d*<sub>6</sub>) δ 164.0 (C), 163.8 (C), 150.2 (d, *J* = 178, C-F), 142.0 (C), 132.5 (C), 131.0 (C), 129.4 (C), 127.6 (CH), 127.6 (CH), 126.0 (CH), 126.0 (CH), 124.3 (C), 115.0 (CH), 110.0 (CH), 109.5 (CH), 100.4 (CH), 21.0 (CH<sub>3</sub>); HREI-MS: *m/z* calcd for C<sub>17</sub>H<sub>12</sub>FN<sub>3</sub>O, [M]<sup>+</sup> 293.0964; Found: 293.0909.

#### 2.3.6. 4-(5-(5-fluoro-1H-indol-2-yl)-1,3,4-oxadiazol-2-yl)phenol (6)

Yield: (91%); <sup>1</sup>HNMR (300 MHz, DMSO *d*<sub>6</sub>): δ 12.36 (s, 1H, NH), 10.87 (s, 1H, OH), 7.98 (d, 2H, *J* = 8.3 Hz), 7.76 (d, 2H, *J* = 8.2 Hz), 7.54 (t, 1H, *J* = 7.1 Hz), 7.32 (d, 1H, *J* = 7.1 Hz); 7.09–7.04 (m, 2H), <sup>13</sup>CNMR (75 MHz, DMSO *d*<sub>6</sub>) δ 164.0 (C), 163.5 (C), 157.5 (C), 150.2 (d, *J* = 175, C-F), 132.5 (C), 129.4 (C), 129.0 (C), 124.2 (C), 116.5 (CH), 116.5 (CH), 116.0 (CH), 116.0 (CH), 115.0 (CH), 110.0 (CH), 100.4 (CH), 109.5 (CH); HREI-MS: *m/z* calcd for C<sub>16</sub>H<sub>10</sub>FN<sub>3</sub>O<sub>2</sub>, [M]<sup>+</sup> 295.0757; Found: 295.0791.

#### 2.3.7. 2-(5-fluoro-1H-indol-2-yl)-5-(3-fluorophenyl)-1,3,4-oxadiazole (7)

Yield: (87%); <sup>1</sup>HNMR (300 MHz, DMSO *d*<sub>6</sub>): δ 12.03 (s, NH, 1H), 7.86 (t, *J* = 7.3 Hz, 1H), 7.73 (d, *J* = 7.1 Hz, 1H), 7.52 (t, *J* = 7.1 Hz, 1H), 7.38–7.27 (m, 2H), 7.24 (d, 1H, *J* = 7.3 Hz); 7.04–6.97 (m, 2H); <sup>13</sup>CNMR (75 MHz, DMSO *d*<sub>6</sub>) δ 164.0 (C), 163.6 (C), 161.5 (d, *J* = 178, C-F), 150.2 (d, *J* = 174, C-F),

132.5 (C), 129.4 (C), 127.9 (C), 127.2 (CH), 124.2 (C), 123.3 (CH), 115.3 (CH), 115.5 (CH), 115.0 (CH), 110.0 (CH), 109.5 (CH), 100.4 (CH); HREI-MS:  $m/z$  calcd for  $C_{16}H_9F_2N_3O$ ,  $[M]^+$  297.0714; Found: 297.0741.

2.3.8. 4-(5-(5-fluoro-1H-indol-2-yl)-1,3,4-oxadiazol-2-yl)benzene-1,3-diol (8)

Yield: (81%);  $^1H$ NMR (300 MHz, DMSO  $d_6$ ):  $\delta$  11.92 (s, 1H, NH), 10.96 (s, 1H, OH), 9.42 (s, 1H, OH), 7.43 (t, 1H,  $J = 7.3$  Hz), 7.32 (d, 1H,  $J = 7.6$  Hz), 7.12 (t, 1H,  $J = 7.3$  Hz), 6.96–6.91 (m, 1H), 6.56–6.47 (m, 2H);  $^{13}C$ NMR (75 MHz, DMSO  $d_6$ )  $\delta$  164.0 (C), 163.5 (C), 159.5 (C), 156.0 (C), 150.2 (d,  $J = 175$ , C-F), 132.5 (C), 130.1 (CH), 129.4 (C), 124.2 (C), 115.0 (CH), 110.0 (CH), 109.5 (CH), 106.1 (CH), 109.5 (CH), 100.4 (CH), 100.0 (C); HREI-MS:  $m/z$  calcd for  $C_{16}H_{10}FN_3O_3$ ,  $[M]^+$  311.0706; Found: 311.0719.

2.3.9. N-(4-(5-(5-fluoro-1H-indol-2-yl)-1,3,4-oxadiazol-2-yl)phenyl)acetamide (9)

Yield: (84%);  $^1H$ NMR (300 MHz, DMSO  $d_6$ ):  $\delta$  11.82 (s, 1H, NH), 11.16 (s, 1H, NH), 7.62 (d, 1H,  $J = 7.6$  Hz), 7.41 (d, 1H,  $J = 7.3$  Hz), 7.16 (s, 1H), 7.04–6.97 (m, 2H), 2.85 (s, 3H,  $CH_3$ );  $^{13}C$ NMR (75 MHz, DMSO  $d_6$ )  $\delta$  168.0 (CO), 164.0 (C), 164.2 (C), 150.4 (d,  $J = 178$ , C-F), 138.0 (C), 132.5 (C), 129.4 (C), 127.5 (CH), 127.5 (CH), 124.5 (C), 121.0 (C), 119.0 (CH), 119.0 (CH), 115.0 (CH), 110.0 (CH), 109.5 (CH), 100.4 (CH), 23.5 ( $CH_3$ ); HREI-MS:  $m/z$  calcd for  $C_{18}H_{13}FN_4O_2$ ,  $[M]^+$  336.1023; Found: 336.1001.

2.3.10. 2-(5-fluoro-1H-indol-2-yl)-5-(4-(trifluoromethyl)phenyl)-1,3,4-oxadiazole (10)

Yield: (80%);  $^1H$ NMR (300 MHz, DMSO  $d_6$ ):  $\delta$  11.72 (s, NH, 1H), 7.92 (d,  $J = 8.4$  Hz, 2H), 7.64–7.62 (m, 3H), 7.18 (t,  $J = 7.2$  Hz, 1H), 6.91 (d,  $J = 8.4$  Hz, 2H);  $^{13}C$ NMR (75 MHz, DMSO  $d_6$ )  $\delta$  164.0 (C), 163.8 (C), 148.0 (C), 150.2 (d,  $J = 178$ , C-F), 132.5 (C), 130.5 (C), 129.4 (C), 127.6 (CH), 127.6 (CH), 126.0 (CH), 126.0 (CH), 124.3 (C), 124.0 (q,  $J = 144$ ,  $CF_3$ ), 115.0 (CH), 110.0 (CH), 109.5 (CH), 100.4 (CH); HREI-MS:  $m/z$  calcd for  $C_{17}H_9F_4N_3O$ ,  $[M]^+$  347.0682; Found: 347.0662.

2.3.11. 2-(3-chlorophenyl)-5-(5-fluoro-1H-indol-2-yl)-1,3,4-oxadiazole (11)

Yield: (91%);  $^1H$ NMR (300 MHz, DMSO  $d_6$ ):  $\delta$  12.31 (s, NH, 1H), 8.06 (d,  $J = 2.0$  Hz, 1H), 7.88 (d,  $J = 8.1$  Hz, 1H), 7.56–7.39 (m, 3H), 7.32 (t,  $J = 6.4$  Hz, 1H), 7.22 (d,  $J = 6.4$  Hz, 1H), 7.05 (t,  $J = 6.2$  Hz, 1H);  $^{13}C$ NMR (75 MHz, DMSO  $d_6$ )  $\delta$  164.0 (C), 163.5 (C), 150.2 (d,  $J = 175$ , C-F), 134.1 (C), 132.5 (C), 129.4 (C), 129.1 (CH), 128.5 (CH), 127.5 (C), 127.0 (CH), 125.1 (CH), 124.2 (C), 115.0 (CH), 110.0 (CH), 109.5 (CH), 100.4 (CH); HREI-MS:  $m/z$  calcd for  $C_{16}H_9ClFN_3O$ ,  $[M]^+$  313.0418; Found: 313.0401.

2.3.12. 2-(5-fluoro-1H-indol-2-yl)-5-(3-methoxyphenyl)-1,3,4-oxadiazole (12)

Yield: (78%);  $^1H$ NMR (300 MHz, DMSO  $d_6$ ):  $\delta$  12.35 (s, NH, 1H), 7.71 (t,  $J = 7.2$  Hz, 1H), 7.62 (d,  $J = 7.1$  Hz, 1H), 7.40–7.32 (m, 3H), 7.24 (t,  $J = 6.7$  Hz, 1H), 7.14 (d,  $J = 6.3$  Hz, 1H), 6.81 (s, 1H), 3.88 (s, 3H,  $OCH_3$ );  $^{13}C$ NMR (75 MHz, DMSO  $d_6$ )  $\delta$  164.0 (C), 163.5 (C), 160.5 (C), 150.2 (d,

$J = 175$ , C-F), 132.5 (C), 129.4 (C), 129.1 (CH), 127.5 (C), 124.2 (C), 119.5 (CH), 115.0 (CH), 114.0 (CH), 111.0 (CH), 110.0 (CH), 109.5 (CH), 100.4 (CH), 55.0 ( $OCH_3$ ); HREI-MS:  $m/z$  calcd for  $C_{17}H_{12}FN_3O_2$ ,  $[M]^+$  309.0914; Found: 309.0897.

2.3.13. 2-(5-fluoro-1H-indol-2-yl)-5-(4-methoxyphenyl)-1,3,4-oxadiazole (13)

Yield: (88%);  $^1H$ NMR (300 MHz, DMSO  $d_6$ ):  $\delta$  12.62 (s, NH, 1H), 7.76 (d,  $J = 8.1$  Hz, 2H), 7.46 (d,  $J = 8.1$  Hz, 2H), 7.38 (t,  $J = 7.3$  Hz, 2H), 7.13 (d,  $J = 6.4$  Hz, 1H), 7.07–7.02 (m, 1H), 3.85 (s, 3H,  $OCH_3$ );  $^{13}C$ NMR (75 MHz, DMSO  $d_6$ )  $\delta$  164.0 (C), 163.5 (C), 160.2 (C), 150.2 (d,  $J = 175$ , C-F), 132.5 (C), 129.4 (C), 129.5 (C), 124.2 (C), 115.5 (CH), 115.5 (CH), 115.0 (CH), 115.0 (CH), 115.0 (CH), 110.0 (CH), 109.5 (CH), 100.4 (CH), 55.3 ( $OCH_3$ ); HREI-MS:  $m/z$  calcd for  $C_{17}H_{12}FN_3O_2$ ,  $[M]^+$  309.0914; Found: 309.0901.

2.3.14. 4-(5-(5-fluoro-1H-indol-2-yl)-1,3,4-oxadiazol-2-yl)benzonitrile (14)

Yield: (82%);  $^1H$ NMR (300 MHz, DMSO  $d_6$ ): 11.66 (s, 1H, NH), 8.12 (d, 2H,  $J = 8.1$  Hz), 7.91 (d, 2H,  $J = 8.1$  Hz), 7.49–7.42 (m, 2H), 7.24 (d, 1H,  $J = 7.3$  Hz), 7.07–7.02 (m, 1H);  $^{13}C$ NMR (75 MHz, DMSO  $d_6$ )  $\delta$  164.0 (C), 163.5 (C), 150.2 (d,  $J = 175$ , C-F), 132.5 (C), 132.0 (CH), 132.0 (CH), 130.0 (C), 129.4 (C), 128.5 (CH), 128.5 (CH), 124.2 (C), 118.0 (–CN), 115.0 (CH), 112.2 (C), 110.0 (CH), 109.5 (CH), 100.4 (CH); HREI-MS:  $m/z$  calcd for  $C_{17}H_9FN_4O$ ,  $[M]^+$  304.0760; Found: 304.0751.

2.3.15. 2-(4-chlorophenyl)-5-(5-fluoro-1H-indol-2-yl)-1,3,4-oxadiazole (15)

Yield: (81%);  $^1H$ NMR (300 MHz, DMSO  $d_6$ ):  $\delta$  11.72 (s, NH, 1H), 7.97 (d,  $J = 8.1$  Hz, 2H), 7.76 (d,  $J = 8.1$  Hz, 2H), 7.46 (d,  $J = 7.4$  Hz, 1H), 7.36–7.30 (m, 2H), 7.12 (t,  $J = 6.8$  Hz, 1H);  $^{13}C$ NMR (75 MHz, DMSO  $d_6$ )  $\delta$  164.0 (C), 163.6 (C), 150.2 (d,  $J = 175$ , C-F), 134.0 (C), 132.5 (C), 129.6 (CH), 129.6 (CH), 129.4 (C), 129.1 (CH), 129.1 (CH), 124.6 (C), 124.2 (C), 115.0 (CH), 110.0 (CH), 109.5 (CH), 100.4 (CH); HREI-MS:  $m/z$  calcd for  $C_{16}H_9ClFN_3O$ ,  $[M]^+$  313.0418; Found: 313.0403.

2.3.16. 2-(5-fluoro-1H-indol-2-yl)-5-phenyl-1,3,4-oxadiazole (16)

Yield: (85%);  $^1H$ NMR (300 MHz, DMSO  $d_6$ ):  $\delta$  9.92 (s, NH, 1H), 7.96 (d,  $J = 7.4$  Hz, 2H), 7.76 (d,  $J = 7.6$  Hz, 2H), 7.44 (t,  $J = 6.6$  Hz, 1H), 7.32–7.7.24 (m, 2H), 7.19 (d,  $J = 7.8$  Hz, 1H), 7.06–7.01 (m, 1H);  $^{13}C$ NMR (75 MHz, DMSO  $d_6$ )  $\delta$  164.0 (C), 163.6 (C), 150.2 (d,  $J = 175$ , C-F), 132.5 (C), 129.4 (C), 129.0 (CH), 129.0 (CH), 128.0 (CH), 127.1 (CH), 127.1 (CH), 124.6 (C), 124.2 (C), 115.0 (CH), 110.0 (CH), 109.5 (CH), 100.4 (CH); HREI-MS:  $m/z$  calcd for  $C_{16}H_{10}FN_3O$ ,  $[M]^+$  279.0808; Found: 279.0796.

2.3.17. 2-(5-fluoro-1H-indol-2-yl)-5-(4-(trifluoromethoxy)phenyl)-1,3,4-oxadiazole (17)

Yield: (89%);  $^1H$ NMR (300 MHz, DMSO  $d_6$ ):  $\delta$  12.02 (s, 1H, NH), 8.13 (d, 2H,  $J = 8.6$  Hz), 7.84 (t, 1H,  $J = 8.2$  Hz), 7.73 (d, 1H,  $J = 8.2$  Hz), 7.48 (d, 2H,  $J = 8.6$  Hz), 7.14–7.07 (m, 2H);  $^{13}C$ NMR (75 MHz, DMSO  $d_6$ )  $\delta$  164.0 (C), 163.8 (C),

150.2 (d,  $J = 178$ , C-F), 150.1 (C), 132.5 (C), 129.4 (C), 129.1 (q,  $J = 148$ , OCF<sub>3</sub>), 128.0 (C), 124.3 (C), 115.6 (CH), 115.6 (CH), 115.0 (CH), 114.5 (CH), 114.5 (CH), 110.0 (CH), 109.5 (CH), 100.4 (CH); HREI-MS:  $m/z$  calcd for C<sub>17</sub>H<sub>9</sub>F<sub>4</sub>N<sub>3</sub>O<sub>2</sub>, [M]<sup>+</sup> 363.0631; Found: 363.0603.

#### 2.4. Antibacterial and anti-biofilm activity

##### 2.4.1. Bacterial strains

The present investigation examined the antibacterial and anti-biofilm activities of compounds A1-A17 against gram-positive methicillin-resistant *Staphylococcus aureus* (MRSA) and gram-negative multidrug-resistant *Pseudomonas aeruginosa* strains. A single colony of fresh bacterial strain was grown overnight in Luria Bertani (LB) broth on a rotary shaker (200 rpm) at 37 °C. In the following step, the bacterial culture was washed with phosphate buffer saline, and the pellet was collected and re-suspended in fresh LB broth.

**2.4.1.1. Minimal inhibitory concentration (MIC).** The MICs values of each compound were determined using serial two-fold microbroth dilution method in a 96 well polystyrene plates against MRSA and *P. aeruginosa* as protocol previously described [26]. The MIC is the lowest concentration of the investigated chemicals at which bacteria did not grow visibly.

**2.4.1.2. Minimum bactericidal concentration (MBC).** Following the MIC analysis, aliquots of 100 µl from wells with no visible bacterial growth (i.e., below MIC value) were inoculated on MHA plates for 24 h at 37 °C. MBC was defined as the concentration that killed 99.99% of bacteria [32].

**2.4.1.3. Effects of compounds on biofilm forming ability of *P. aeruginosa* and MRSA.** The antibiofilm potential of each compound was quantitatively investigated against *P. aeruginosa* and MRSA strains by using microtitre culture plate assay [33]. Briefly, 20 µl fresh cultures of *P. aeruginosa* and MRSA strains (1x 10<sup>7</sup> CFU/ml) were added into 180 µl of increasing concentrations of each compound (0.25–4 mg/ml) in a 96 well sterile polystyrene flat bottom microtitre plate and were incubated without shaking at 37 °C for 24 h. After 24 h of incubation, bacterial suspensions from each well were completely decanted and the wells were washed twice with sterile phosphate buffer saline (PBS, 1X) and left for complete air drying. Each sample was then stained with 0.25% crystal violet solution for 30 min. Following staining, the wells were rinsed with PBS, the excess dyes were removed and then bound stain was solubilize with 95% ethanol. Finally, the absorbance was measured at 595 nm using a microtitre plate reader and percent biofilm inhibition was calculated by using following equation:

$$\% \text{ Biofilm inhibition} = \left\{ \frac{(\text{OD of control} - \text{OD of tested samples})}{(\text{OD of control})} \right\} \times 100$$

#### 2.5. Molecular docking analysis

##### 2.5.1. Preparation compounds for the docking

ChemDraw 19.1.0.8 (<http://www.cambridgesoft.com/pki/>) was used to draw the chemical structures of selected compounds. CORINA's classic 3D structure generator server generates

3D structures using the chemical canonical SMILES IDs of the selected substances ([https://www.mnam.com/online\\_demo/corina\\_demo](https://www.mnam.com/online_demo/corina_demo)). Remdesivir (REM) structure was taken from the DrugBank database (<https://go.drugbank.com/drugs/DB14761>) [27] and set as standards for the study. Furthermore, Discovery Studio visualizer 2020 [28] was used to complete the energy minimization process for the produced 3D structures of selected compounds using the CHARMM force field [34].

##### 2.5.2. Preparation of 3D bacterial peptidoglycan structure and SARS-CoV-2 main protease

The 3D structure of bacterial peptidoglycan (PDB ID: 2MTZ) and SARS-CoV-2 main protease (PDB ID: 6LU7) was retrieved from Protein Data Bank [29,35,36,37]. Then, for the energy reduction process, the CHARMM force field was applied to both 3D structures [34]. For the aforementioned manipulation of 3D structures, Discovery Studio visualizer 2020 was employed [28].

##### 2.5.3. Molecular docking assisted virtual screening

We have utilized PyRx tool [30] which can perform major phases during molecular interaction like receptor and ligand molecules preparation, docking using AutoDock Vina tool [31]. Initially, the PyRx tool was used to screen seventeen synthesized compounds (C1-C17) for their binding affinity against SARS-CoV2 (PDB ID: 6LU7). The PyRx tool generates interaction analysis results quickly [30,38].

##### 2.5.4. AutoDock calculation

Based on the PyRx virtual screening and obtained MIC values of C1-C17 compounds against tested bacteria, compounds C6, C7, C8, C10 and C11 were chosen for docking studies with bacterial peptidoglycan and SARS-CoV2 Main Protease using the AutoDock tool. In order to cover the maximum area within the grid box of 60x60x60 Å that can accommodate the active site key residues His41, Cys145, and Glu166. Active site were identified and extracted through literature survey and from the PDB ID:6LU7 structure, the grid center point coordinates X, Y, and Z were set to -15.253, 14.22, 65.592 for PDB ID:6LU7 and 6.211, -5172, 12.171, respectively, for PDB ID:2MTZ (Entity3) [36,39,35].

##### 2.5.5. ADME, Drug-likeness and toxicity assessment

The SwissADME online tool (<http://www.swissadme.ch>) was used to determine the absorption, delivery, metabolism, and excretion (ADME), drug-likeness, and pharmacokinetics properties of compounds C6, C7, C8, C10, and C11 [40,41]. Toxicity analysis was then carried out using the pkCSM online server <http://biosig.unimelb.edu.au/pkcs/>, which can easily determine and predict the toxicity properties of compounds of interest [42].

##### 2.5.6. Target prediction

Target prediction is a potentially useful tool for identifying biological macromolecules such as proteins and enzymes in small drug-like compounds. We used free online Swiss Target Prediction to make this prediction (<http://www.swisstargetprediction.ch>) [43].

### 3. Results and discussion

#### 3.1. Chemistry

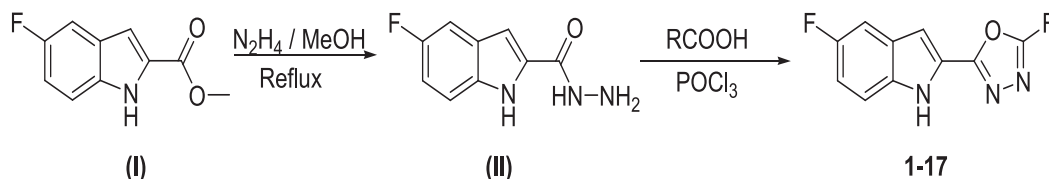
The 5-fluoro-indole based oxadiazoles (**1–17**, Scheme 1) synthesized [44]. The methyl 5-fluoro-1H-indole-2-carboxylate (I) heated under reflux with methanolic hydrazine solution for six hours to provide 5-fluoro-1H-indole-2-carbohydrazide (II) followed by treating 5-fluoro-1H-indole-2-carbohydrazide (II) with various aromatic carboxylic acids in the presence of

$\text{POCl}_3$  to accomplish indole based oxadiazoles (**1–17**). Categorization of all products **1–17** was performed using different spectroscopy methods (Supplementary file 1).

#### 3.2. Investigation of antibacterial activity of 5-fluoro-indole based oxadiazoles (**1–17**)

##### 3.2.1. MIC and MBC assessment

Methicillin-resistant *S. aureus* (MRSA) and multidrug-resistant *P. aeruginosa* (MDR-PA) causes serious problems in healthcare settings. These two bacterial strains are the major

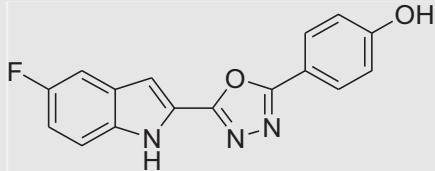
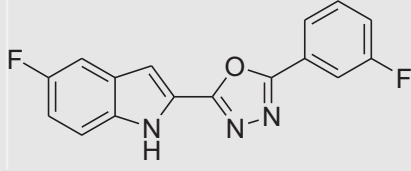
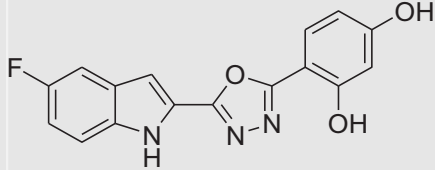
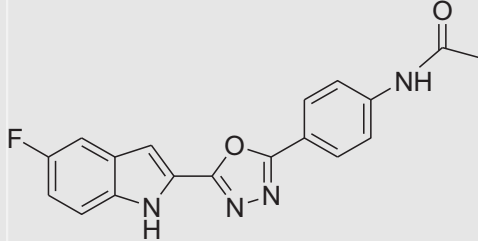
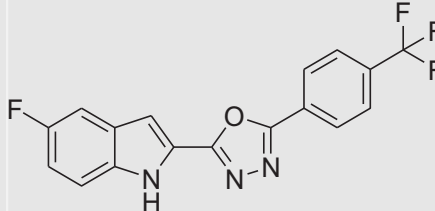
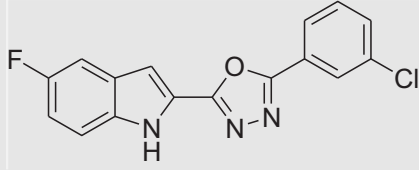
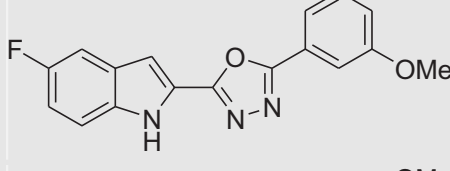
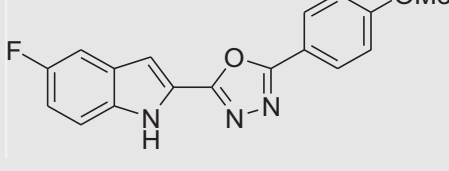


**Scheme 1** synthesis of 5-fluoro-indole based oxadiazoles (**1–17**).

**Table 1** Minimum inhibitory and minimum bactericidal concentration (MIC and MBC in mg/ml) of A series compounds against drug resistant *P. aeruginosa* and MRSA.

No.	Structures	MDR-PA		MRSA	
		MIC	MBC	MIC	MBC
1		8	16	2	4
2		NA	NA	2	4
3		NA	NA	8	16
4		NA	NA	NA	NA
5		NA	NA	4	8

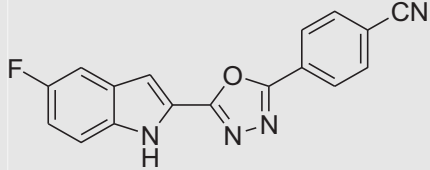
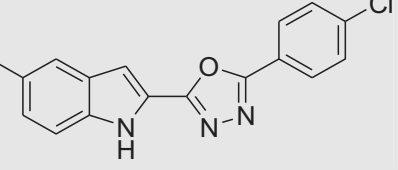
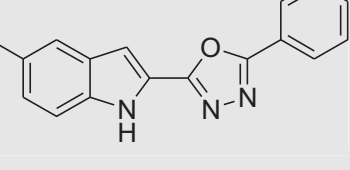
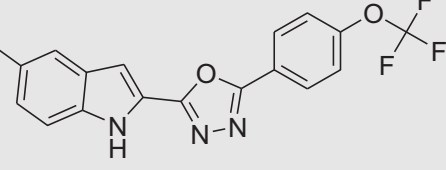
**Table 1** (continued)

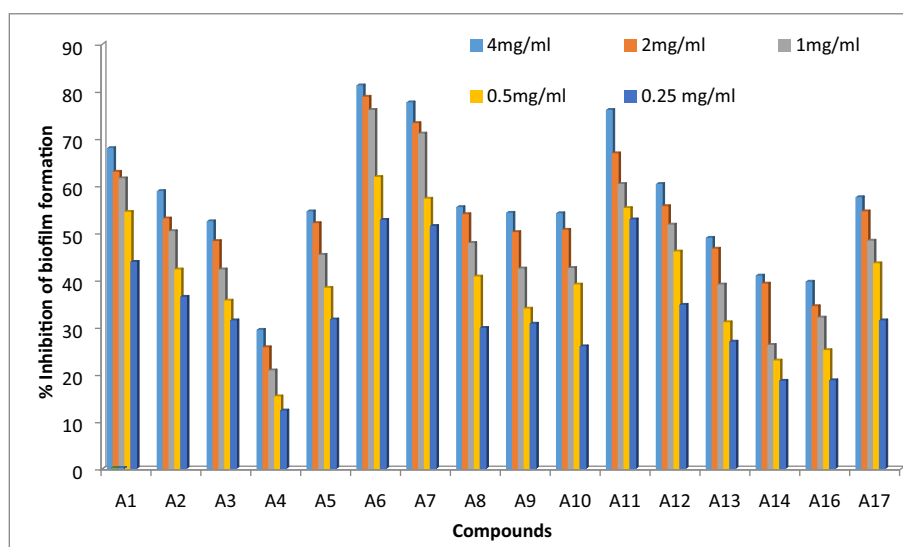
No.	Structures	MDR-PA		MRSA	
		MIC	MBC	MIC	MBC
6		4	8	1	2
7		4	8	1	2
8		4	16	2	4
9		8	16	2	4
10		4	16	2	4
11		4	16	1	2
12		8	16	2	4
13		8	16	8	16

(continued on next page)



**Table 1** (continued)

No.	Structures	MDR-PA		MRSA		
		MIC	MBC	MIC	MBC	
14	 <chem>N#CC1=CC=C(C=C1)C2=NN=C(C2)c3cc(F)ccc3N</chem>	4-(5-(5-fluoro-1H-indol-2-yl)-1,3,4-oxadiazol-2-yl) benzonitrile	NA	NA	8	16
15	 <chem>Clc1ccc(cc1)C2=NN=C(C2)c3cc(F)ccc3N</chem>	2-(4-chlorophenyl)-5-(5-fluoro-1H-indol-2-yl)-1,3,4-oxadiazole	NA	NA	8	16
16	 <chem>c1ccc(cc1)C2=NN=C(C2)c3cc(F)ccc3N</chem>	2-(5-fluoro-1H-indol-2-yl)-5-phenyl-1,3,4-oxadiazole	NA	NA	8	16
17	 <chem>COc1ccc(cc1)C2=NN=C(C2)c3cc(F)ccc3N</chem>	2-(5-(5-fluoro-1H-indol-2-yl)-5-(4-(trifluoromethoxy)phenyl)-1,3,4-oxadiazole	NA	NA	4	8

**Fig. 1** Effects of 1–17 compounds on biofilm formation abilities of MRSA.

cause of nosocomial infection worldwide that result significant increases rate of both mortality and morbidity. Thus, the increasing clinical importance of antibiotic-resistant in bacterial pathogens is a great challenge for the researchers to develop novel broad-spectrum antimicrobial drug agents. Recently, heterocyclic indole and oxadiazoles derivatives com-

pounds have been reported as anticancer, antibacterial, antifungal, antiviral, antituberculosis potentialities [45,46,47,48].

In this present study, the antibacterial property of 5-fluoroindole based oxadiazoles (**1–17**) was examined against drug resistant gram-negative bacteria MDR-PA and gram-positive

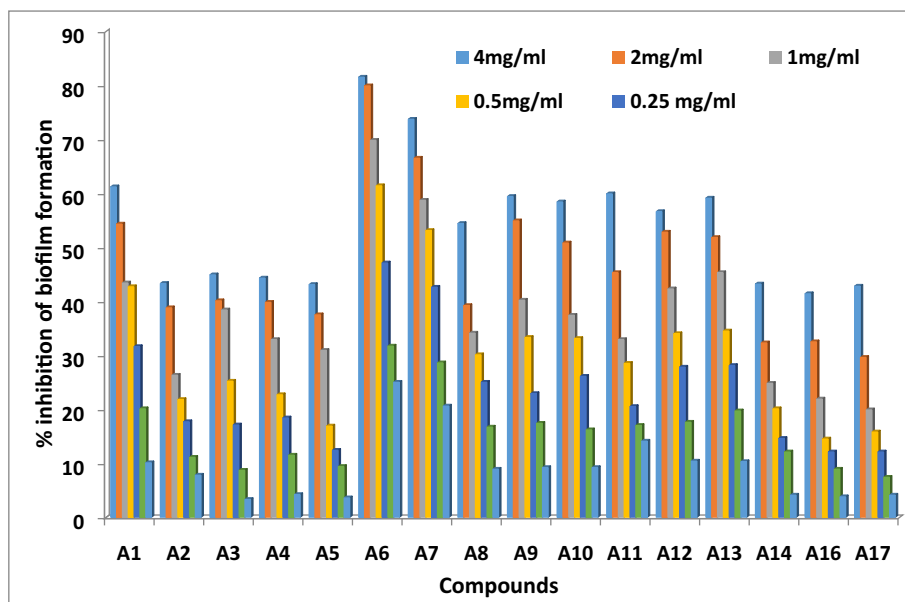


**Fig. 2** Effects of 1–17 compounds on biofilm formation abilities of multidrug-resistant *P. aeruginosa*.

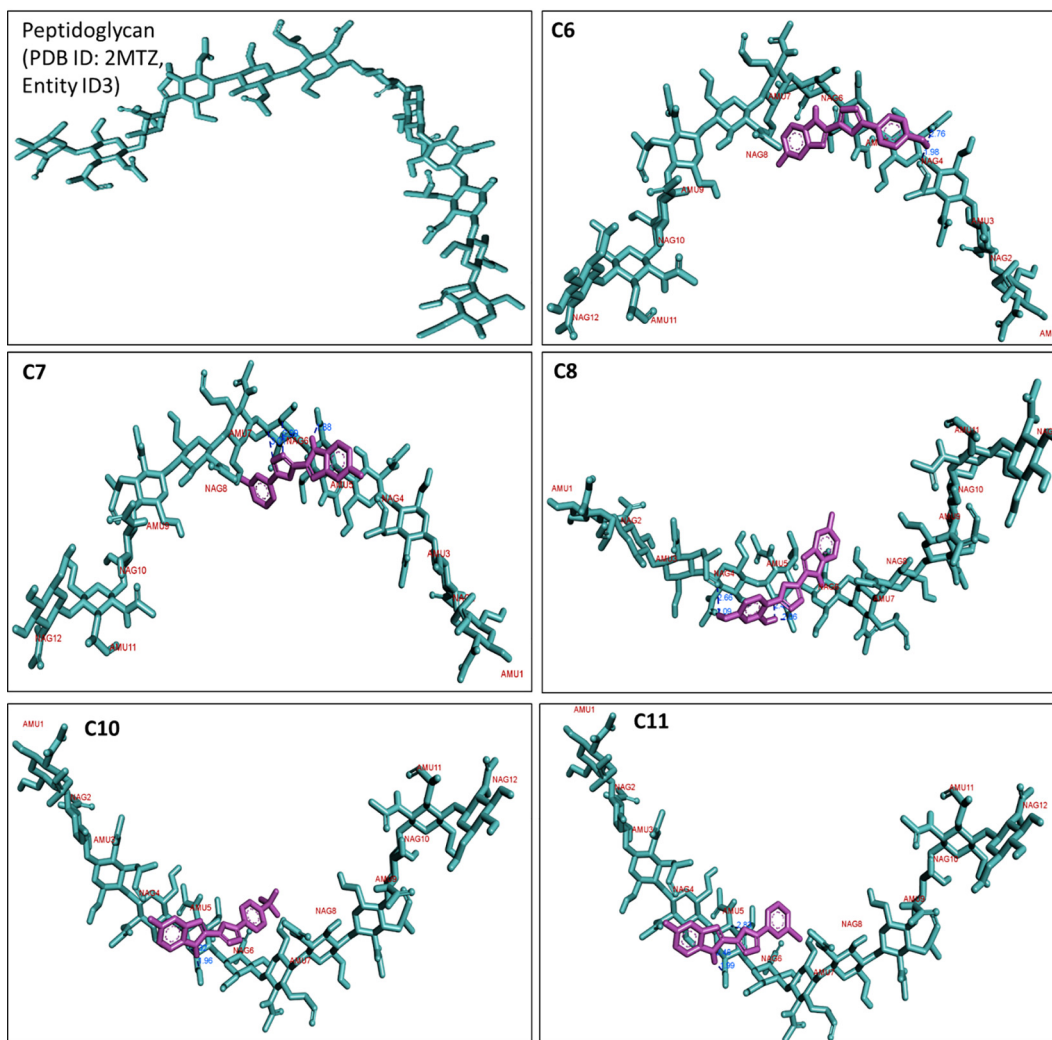


**Fig. 3** 3D visualization of C6, C7, C8, C10 and C11 (Shown by pink color in stick pattern) interaction with bacterial cell wall peptidoglycan shown by turquoise color and stick pattern (PDB ID: 2MTZ Entity 3).

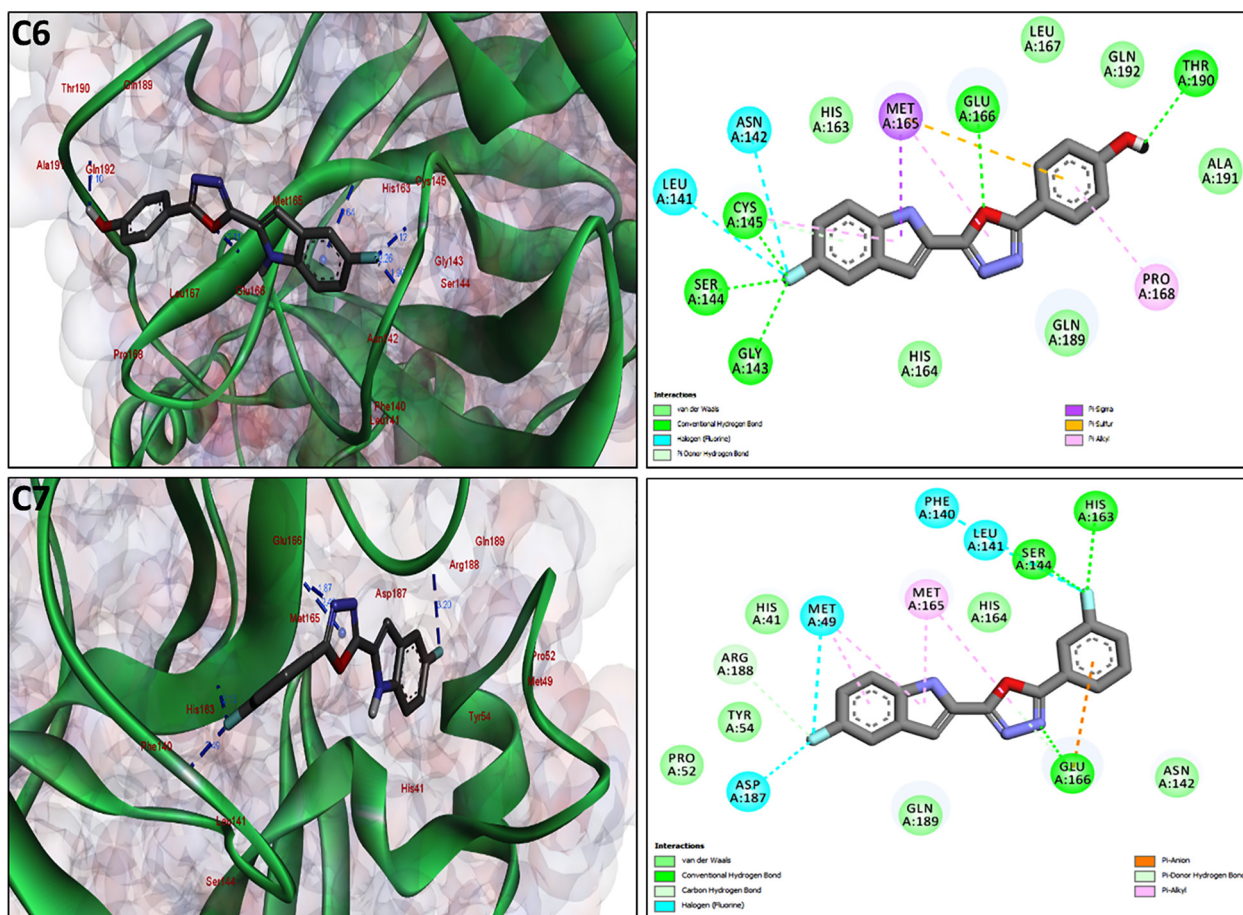


**Fig. 4** 3D and 2D visualization of molecular interaction between compounds C6 and C7 (shown by grey stick pattern in the center) and SARS-CoV-2 main protease (PDB ID: 6LU7) shown in green color. Formed hydrogen bonds are shown by blue dotted lines. 2D graphics showing several other types of interaction with different color dotted lines and interacting amino acid residues shown in spheres. All graphics were generated by Discovery Studio Visualizer 2020.

MRSA by determining the MIC and MBC values using microbroth dilution method. The MICs and MBCs values of tested compounds were shown in Table 1. It was found that the compounds A2 to A5 and A14 to A17 did not show any activity against MDR-PA upto 16 mg/ml of concentrations. On the other hand, we found that all compound shows good antibacterial activity against gram-positive MRSA except A4. The lowest MIC and MBC value recorded was 1 and 2 mg/ml, respectively, for compound A6, A7 and A11 against MRSA; whereas for *P. aeruginosa* the lowest MIC and MBC was 4 and 8 mg/ml, respectively for compound A6 and A7 (Table 1). The MIC and MBC values clearly shows that the compound A6 and A7 shows maximum antibacterial activity against MDR-PA, whereas A6, A7 and A11 shows highest activity against MRSA (Table 1). It has been found that tested compounds were more effective against gram-positive MRSA than gram-negative MDR-PA. These differences may be due to the structural differences in cell wall of these two types of bacteria. The cell wall of gram-positive bacteria i.e., MR- *S. aureus* has a single layer of peptidoglycans whereas gram-negative bacteria i.e., MDR- *P. aeruginosa* has multilayered cell wall, that possess an outer membrane, periplasmic space and lipopolysaccharides, which is absent in gram-positive bacteria.

**Table 2** PyRx Virtual screening results shown binding affinity of C1-C17 compounds against SARS-CoV-2 (PDB ID: 6LU7).

Compounds	Binding Energy (Kcal/mol)
C1	-7.6
C2	-7.5
C3	-7.5
C4	-7.6
C5	-7.5
C6	-7.7
C7	-7.6
C8	-7.7
C9	-7.4
C10	-7.7
C11	-7.6
C12	-7.4
C13	-7.3
C14	-7.6
C15	-7.5
C16	-7.5
C17	-7.5

**Table 3** Showing results obtained after performing Molecular docking between C6,C7,C8,C10,C11 and Entity ID 3 (peptidoglycan hexamuropeptide) (PDB ID: 2MTZ) generated by AutoDock tool. In hydrogen bonds formation details column UNK1 = selected compounds.

Compounds	Estimated Free Energy of Binding (kcal/mol)	Estimated Inhibition Constant (Ki)	Hydrogen bonds formation details	Hydrogen bonds length (Angstrom)	Interacting residues
C6	-6.26	25.96 $\mu$ M	:UNK1:H24 - H:AMU3:O10 :UNK1:H24 - H:NAG4:O7	1.9843 2.75522	AMU3,NAG4
C7	-6.10	33.74 $\mu$ M	:UNK1:H15 - H:AMU5:O6 H:NAG6:C4 -:UNK1:N9 H:NAG6:C6 -:UNK1:N10	1.87652 3.01328 2.98948	AMU5, NAG6
C8	-6.60	14.60 $\mu$ M	:UNK1:H25 - H:AMU3:O10 :UNK1:H25 - H:NAG4:O7 :UNK1:H32 - H:AMU5:O5 :UNK1:H32 - H:AMU5:O6	2.66374 2.09185 2.49231 2.05858	AMU3,NAG5, AMU5,
C10	-5.68	68.40 $\mu$ M	:UNK1:H18 - H:AMU5:O5 :UNK1:H18 - H:AMU5:O6	2.32277 1.95627	AMU5
C11	-5.76	60.18 $\mu$ M	:UNK1:H15 - H:AMU5:O5 :UNK1:H15 - H:AMU5:O6 H:AMU5:C2 -:UNK1:O12	2.45996 1.99349 2.82597	AMU5

The resistance of gram-negative bacteria towards antibacterial agents due to their membranes being more lipophilic, which acts as a barrier for a variety of antimicrobial agents and thus hydrophilic substances were believed to be incapable of penetrating these bacteria's cell membranes. On the other hand, gram positive bacteria lack such an outer layer and an intricate cell wall structure and therefore, antibacterial agents are capable of easily destroying the gram-positive bacteria's cell wall and cytoplasmic membrane, resulting in the leakage of cytoplasm content that may led to the death of bacteria [49,50].

### 3.3. Antibiofilm potential against MRSA and MDR-PA biofilm

MRSA and *P. aeruginosa* propensity to build biofilms is a critical virulence factor linked to nosocomial infections. These bacterial strains have the ability to form biofilm on a various surface especially on implanted medical devices such as mucus plugs, artificial implants, pacemakers, prosthetic joints, catheters, endotracheal tubes, intra-uterine devices, mechanical heart valves, tympanostomy tubes, urinary catheters, and voice prostheses and contact lenses [51,52]. Bacteria that colonize medical devices usually aggregate and grow in the form of biofilm. Biofilms are complex microbial communities that are encased in a matrix of extracellular polymeric substances, which are irreversibly attached to these surfaces. The structure and physiological features of a biofilm contribute to the characteristic resistance of biofilm-forming bacteria to antimicrobial agents, such as antibiotics or disinfectants. Importantly, biofilm also provide a shield from the biological attacks that occur in the form of host defenses [51].

In the present study, antibiofilm activity of 1–17 was investigated against MRSA and MDR- *P. aeruginosa* biofilms using crystal violet assay by measuring absorbance at 595 nm. Figs. 1 and 2 clearly shows that tested compounds restrict biofilm formation in a dose-dependent manner. A6, A7 and A11 showed maximum inhibition of biofilm formation by MRSA in compared to other tested compounds. It was found that at 4 mg/ml; A6, A7 and A11 inhibit MRSA biofilm formation by

81.1, 77.5 and 75.9%, respectively (Fig. 1); whereas in case of *P. aeruginosa*; A6 and A7 showed maximum biofilm inhibition and it was found that at 4 mg/ml, A6 and A7 inhibit biofilm formation by 81.5 and 73.7%, respectively (Fig. 2). The Figs. 1 and 2 clearly demonstrate that the A6, A7 and A11 suppressed MRSA biofilm formation more efficiently than the biofilm of *P. aeruginosa*. The plausible mechanism for interfering biofilm formation of MRSA and MDR-PA by tested compounds might be due to the disruption of adherence and colonization of bacterial cells. Fig. 3..

### 3.4. Molecular docking studies of selected compounds with bacterial peptidoglycan

The docking study was used to validate the antibacterial activity of selected compounds by investigating their binding affinity with bacterial peptidoglycans. Compounds A6, A7, A8, A10, and A11 were chosen for further deep analysis against bacterial peptidoglycan (PDB ID: 2MTZ, Entity ID 3) using the AutoDock tool, based on antibacterial activity (MIC values, Table 1). Not only does the cell wall protect the contents of the cell from adverse conditions, but it also provides rigidity, form, and, most significantly, specifies the cellular structure, which is critical for virulence and pathogenicity. The bacterial cell wall is composed of peptidoglycan, a long-chain polymer of sugars and amino acids composed of alternating residues of -(1,4) linked N-acetylglucosamine (NAG) and N-acetylmuramic acid (NAM).

Based on our antibacterial findings (MIC), we used docking analysis to examine the binding affinity and possible interaction of compounds A6, A7, A8, A10, and A11 with bacterial peptidoglycan. The results of the docking studies of A6, A7, A8, A10, and A11 compounds with bacterial peptidoglycan (PDB ID: 2MTZ, Entity ID 3) and their binding affinities were shown in Table 3 and Fig. 4. Compounds A6, A7, A8, A10, and A11 had binding affinity ranging from -5.68 to -6.6 kcal/mol, indicating their high efficacy. The best inhibitor was the C8 molecule, which had the highest binding affinity

**Table 4** Showing results obtained after performing Molecular docking between C6, C7,C8,C10,C11 and SARS CoV-2 Main Protease (PDB: 6LU7) generated by AutoDock tool. In hydrogen bonds formation details column UNK1 = selected compounds.

Compounds	Estimated Free Energy of Binding (kcal/mol)	Estimated Inhibition Constant (Ki)	Hydrogen bonds formation details	Hydrogen bonds length (Angstrom)	Amino acid residues involved in hydrophobic interaction
<b>Control (REM)</b>	-6.41	19.91 $\mu$ M	A:HIS163:HE2 -:UNK1:N23 :UNK1:H66 - A:PHE140:O A:PRO168:CA -:UNK1:O9 A:HIS172:CD2 -:UNK1:N23 :UNK1:C24 - A:ASN142:OD1	2.33474 2.20138 3.22769 3.2802 3.07952	His41,Phe140,Leu141,Asn142,Gly143,Cys145,His163,Met165,Glu166,Leu167,Pro168,His172,Gln189,Thr190,Gln192
<b>C6</b>	-7.78	2.00 $\mu$ M	A:GLY143:HN -:UNK1:F20 A:SER144:HN -:UNK1:F20 A:CYS145:HN -:UNK1:F20 A:GLU166:HN -:UNK1:O12 :UNK1:H24 - A:THR190:O A:CYS145:SG -:UNK1	2.26268 1.89569 2.1249 2.11445 2.10202 3.63783	Leu141,Asn142,Gly143,Ser144,Cys145,His163,His164,Met165,Glu166,Leu167,Pro168,Gln189,Thr190,Ala191,Gln192
<b>C7</b>	-7.61	2.63 $\mu$ M	A:SER144:HG -:UNK1:F1 A:HIS163:HE2 -:UNK1:F1 A:GLU166:HN -:UNK1:N9 A:ARG188:CA -:UNK1:F20 A:GLU166:HN -:UNK1	2.48909 2.12637 1.87134 3.19561 2.49192	His41, Met49, Pro52, Tyr54, Phe140, Leu141, Ser144, His163, Met165, Glu166, Asp187, Arg188, Gln189
<b>C8</b>	-7.67	2.40 $\mu$ M	A:GLY143:HN -:UNK1:F18 A:SER144:HN -:UNK1:F18 A:CYS145:HN -:UNK1:F18 A:GLU166:HN -:UNK1:O10 A:GLN192:HN -:UNK1:O1 :UNK1:H25 - A:GLN192:O :UNK1:H32 - A:GLU166:O A:CYS145:SG -:UNK1	2.01845 2.14966 2.13917 2.07953 1.72923 2.14503 2.12933 3.47693	Leu141,Gly143,Ser144,Cys145,His163, Met165,Glu166,Pro168,Gln189,Thr190, Gln192
<b>C10</b>	-6.75	11.30 $\mu$ M	A:TYR54:HH -:UNK1:F23 A:ASN142:HN -:UNK1:F4 A:GLU166:HN -:UNK1	2.72626 2.82779 2.34003	His41, Met49, Tyr54, Phe140, Leu141, Asn142, Met165, Glu166, Asp187, Arg188, Gln189
<b>C11</b>	-7.78	1.97 $\mu$ M	A:TYR54:HH -:UNK1:F20 :UNK1:H15 - A:HIS164:O A:GLU166:HN -:UNK1	2.52692 1.83537 2.39606	His41, Tyr54, Phe140, Leu141, Asn142, Ser144, His163, His164, Met165, Glu166, Asp187, Gln189

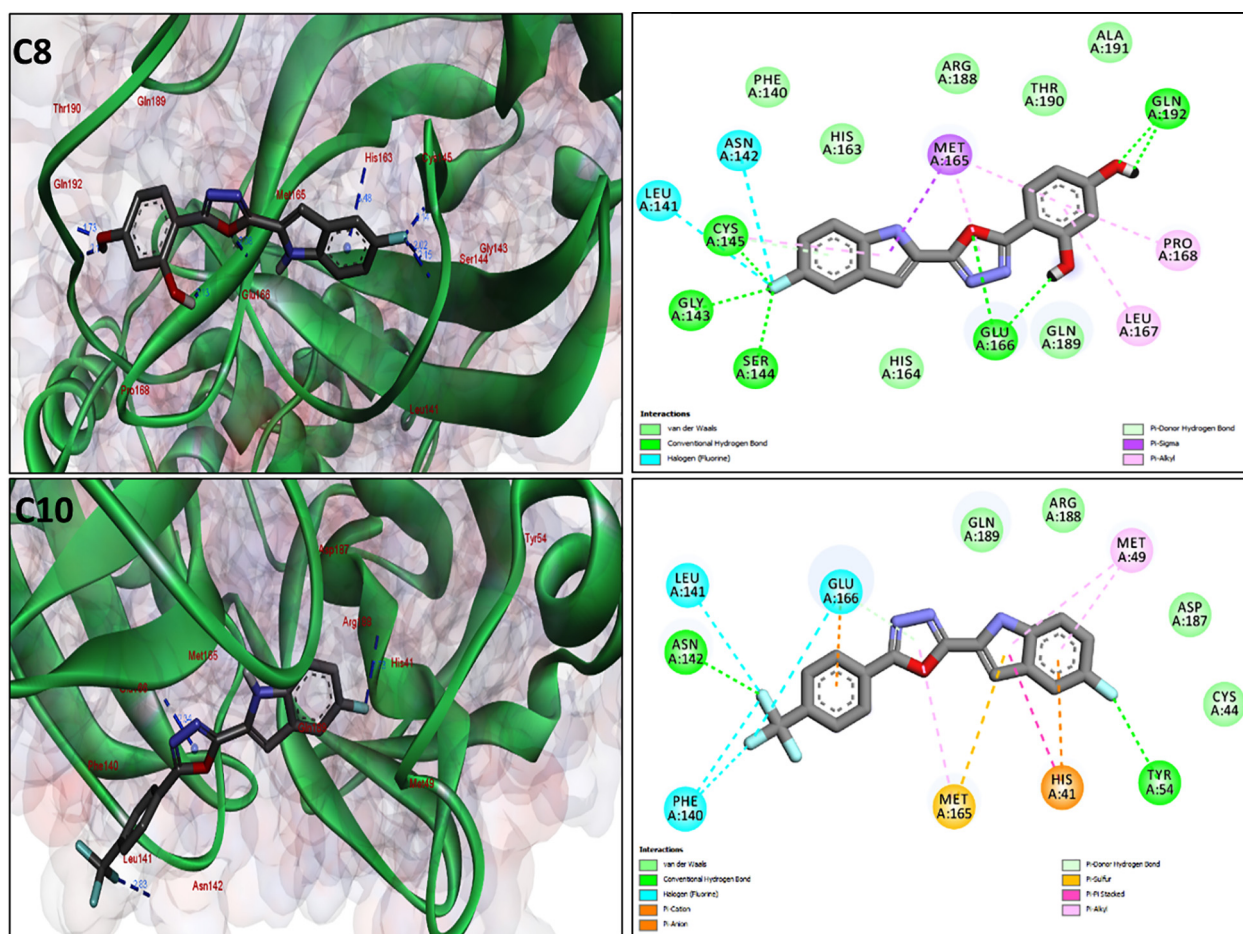


**Fig. 5** 3D and 2D visualization of molecular interaction between selected compounds C8 and C10 (shown by grey stick pattern in the center) and SARS-CoV-2 main protease (PDB ID: 6LU7) shown in green color. Formed hydrogen bonds are shown by blue dotted lines. 2D graphics showing several other types of interaction with different color dotted lines and interacting amino acid residues shown in spheres. All graphics were generated by Discovery Studio Visualizer 2020.

of  $-6.6$  kcal/mol and lowest inhibition Constant ( $K_i$ ) of  $14.60$   $\mu\text{M}$ . The A8 molecule formed 4 hydrogen bonds; 3 with N-acetylmuramic acid (i.e., AMU3, AMU5 and AMU5) and 1 with N-acetylglucosamine (NAG5) residues of peptidoglycan, respectively (Fig. 4 and Table 3). On the other hand, compounds A6 and A10 formed 2 hydrogen bonds, while compound A7 and A11 formed 3 hydrogen bonds (Table 3 and Fig. 4), respectively, indicating that these interactions could be connected with damaging and irreversible conformational changes in the bacteria's cell wall structural proteins, which could result in the bacteria's death. Our findings imply that the synthesized compounds could be a good choice for antibiotic therapy and prevention of biofilm-related microbial infections.

### 3.5. Molecular docking studies of selected compounds with COVID-19 main protease

A6, A7, A8, A10, and A11 were chosen for further deep analysis against main protease of SARS-CoV2 (PDB ID: 6LU7), using the AutoDock tool, based on their binding affinity (Kcal/mol) obtained by PyRx virtual screening tool (Table 2) and antibacterial activity results. The molecular docking analysis was used to assess the anti-SARS-CoV2 efficacy of synthe-

sized indole-based-oxadiazole derivatives by examining the binding modalities and orientation of the ligands in the receptor pocket of the main protease. The binding affinities of the synthesized compounds with the main protease were shown in Table 1. The binding affinity of complexes was found to range between  $-6.75$  and  $-7.78$  kcal/mol, indicating their high potency. A6 and A11 were found to be the most effective inhibitors, with a binding affinity of  $-7.78$  kcal/mol. Furthermore, the compounds studied in this work have a higher binding affinity than Remdesivir, a common antiviral medication with a binding affinity of  $-6.41$  kcal/mol (Table 4).

A6 molecule formed 6 conventional hydrogen bonds with GLY143, SER144, CYS145, GLU166, THR190, and CYS145 amino acid residues in the active pocket of the target as shown in Fig. 4. The fluorine substituent ( $-F$ ) attached to oxadiazol ring formed 2 hydrophobic interactions (halogen) with Leu141 and Asn142. Some other hydrophobic interactions such as Pi-alkyl (with Cys145, Met165 and Pro168), Pi-sigma and Pi-sulfur (with Met 165), van der Waals (with Leu167, Ala191 and Gln 192) and carbon-hydrogen interaction (His164 and Gln189) was also observed (Fig. 4 & Table 4).

A7 showed a significant binding affinity with main protease of SARS-CoV2 (PDB ID: 6LU7) with total binding energy  $-7.61$  kcal/mol, inhibition constant  $2.63$   $\mu\text{M}$ , 5H-bonds (A:

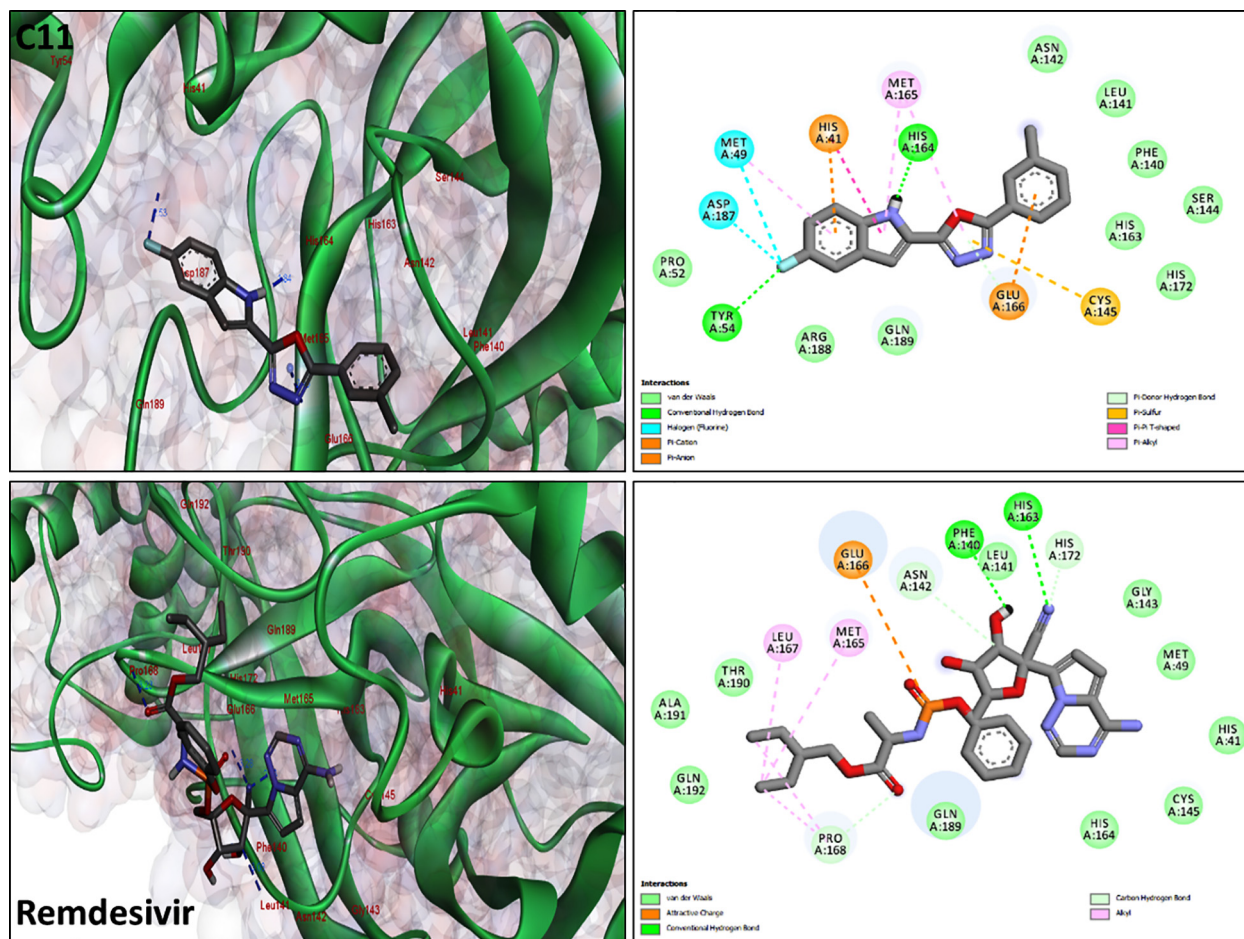


**Fig. 6** 3D and 2D visualization of molecular interaction between selected compounds C11 and standard drug REM (shown by grey stick pattern in the center) and SARS- CoV-2 main protease (PDB ID: 6LU7) shown in green color. Formed hydrogen bonds are shown by blue dotted lines. 2D graphics showing several other types of interaction with different color dotted lines and interacting amino acid residues shown in spheres. All graphics were generated by Discovery Studio Visualizer 2020. ADME, Drug-likeness and Toxicity profile.

**Table 5** ADME prediction data obtained from SwissADME online tool (GI = Gastro intestinal, BBB = Blood Brain Barrier, Pgp = P glycoprotein, CYP = Cytochrome, log Kp = skin permeation).

Compounds	GI absorption	BBB permeant	Pgp substrate	CYP1A2 inhibitor	CYP2C19 inhibitor	CYP2C9 inhibitor	CYP2D6 inhibitor	CYP3A4 inhibitor	log Kp (cm/s)
C6	High	Yes	Yes	Yes	Yes	No	Yes	No	-6.17
C7	High	Yes	Yes	Yes	Yes	No	Yes	No	-5.85
C8	High	No	Yes	No	No	No	Yes	Yes	-6.51
C10	High	Yes	Yes	Yes	Yes	No	No	No	-5.6
C11	High	Yes	Yes	Yes	Yes	No	Yes	No	-5.58

SER144:HG-:UNK1:F1, A:HIS163:HE2-:UNK1:F1, A:GLU166:HN-:UNK1:N9, A:ARG188:CA-:UNK1:F20, and A:GLU166:HN-:UNK1) formed with lengths of 2.4, 2.1, 1.8, 3.1 and 2.4 Angstrom (Å), respectively. The amino acids involved in hydrophobic interaction were shown in Table 4 and Fig. 4. A number of other interactions were also observed such as Glu166 formed Pi-Anion, Met49 and Met165 was involved in Pi-Alkyl bond interactions, while, fluorine substituent (-F) attached to oxadiazol ring at position 3 and 5

were involved in halogen bond interactions with Met49, Asp187 and Phe140, Leu141, respectively.

A8 has shown a binding affinity -7.67 kcal/mol, inhibition constant 2.40  $\mu$ M, eight (8) H-bond (A:GLY143:HN-:UNK1:F18, A:SER144:HN-:UNK1:F18, A:CYS145:HN-:UNK1:F18, A:GLU166:HN-:UNK1:O10, A:GLN192:HN-:UNK1:O-:UNK1:H25- A:GLN192:O-:UNK1:H32-A:GLU166:O, and A:CYS145:SG-:UNK1) formed with the lengths of 2.01, 2.1, 2.1, 2.07, 1.7, 2.1, 2.1, and 3.4 Å, respectively. The amino

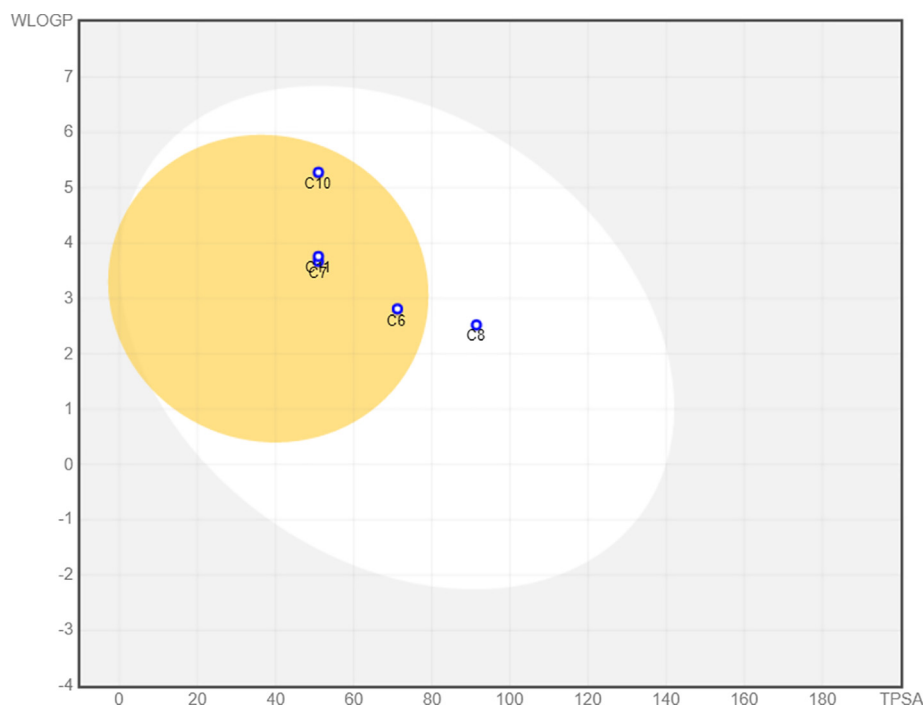


**Fig. 7** BOILED-Egg graph of compounds C6, C7, C8, C10 and C11. Yellow BOILED-Egg's yolk denotes that molecules are passively permeate through the blood–brain barrier (BBB), White part of BOILED-Egg's denotes molecules are passively absorbed by the gastrointestinal tract. Blue dots showing molecules predicted to be effluated from the central nervous system by the P-glycoprotein.

acids involved in hydrophobic interaction were shown in Fig. 5 & Table 4. After analyzing complex interaction, it was also found that Cys145, Met165, Leu167 and Pro168 were involved in forming Pi-Alkyl bonds. Met165 was involved in Pi-Sigma contact. Fluorine substituent (–F) attached to oxadiazol ring at position 5 were involved in halogen bond formation with Leu141 and Asn142. forming Alkyl and Pi-Alkyl bonds (Fig. 5 & Table 4).

A10 interacted with  $-6.75$  kcal/mol, inhibition constant  $11.30$   $\mu\text{M}$ , 3H-bonds A:TYR54:HH -:UNK1:F23, A:ASN142:HN -:UNK1:F4 and A:GLU166:HN -:UNK1) with the length of 2.7, 2.8 and 2.3 Å, respectively. The amino acids involved in hydrophobic interaction were shown in Fig. 5 & Table 4. Apart from traditional conventional bonds other types of interactions were also observed. Met49 and Met165 formed Pi-Alkyl bond, Met165 formed Pi-sulfur bond, His41 formed Pi-Pi stacked and Pi-Anion, Glu166 formed Pi-cation, while, fluorine substituent (–F) attached to oxadiazol ring at position 4 involved in halogen-fluorine interaction with Phe140, Leu141 and Glu166, respectively (Fig. 5 & Table 4).

A strong binding energy has also been observed during A11 and main protease of SARS-CoV2 (PDB ID: 6LU7) interaction. It was  $-7.78$  kcal/mol, inhibition constant  $1.97$   $\mu\text{M}$  and 3H-bonds (A:TYR54:HH -:UNK1:F20,:UNK1:H15 - A: HIS164:O and A:GLU166:HN -:UNK1) formed with the length of 2.5, 1.8 and 2.3 Å, respectively. The amino acids involved in hydrophobic interaction were shown in Fig. 6 & Table 4. C11 shows a number of some other types of interactions such one Pi-cation and Pi-Pi T-shaped (with amino acid residues of His41), three Pi-alkyl (with amino acid residues of

Met49, His 164 and Met165), one Pi-anion (with amino acid residue Glu166), one Pi-sulfur (with Cys145), two halogen-fluorine (with amino acid residues of Met49 and Asp187) (Fig. 6 & Table 4).

In this study, the interaction energies examined by in silico analysis against major protease (PDB: 6LU7) with synthetic compounds (A6, A7, A8, A10, and A11) have a greater binding affinity ( $-6.75$  to  $-7.78$  kcal/mol) than conventional antiviral medicine Remdesivir, which has a binding affinity of  $-6.41$  kcal/mol. Remdesivir has inhibition constant of  $19.91$   $\mu\text{M}$  and formed five (5) hydrogen bonds (A:HIS163:HE2 -:UNK1:N23,:UNK1:H66 - A:PHE140:O, A:PRO168:CA -:UNK1:O9, A:HIS172:CD2 -:UNK1:N23 and:UNK1:C24 - A:ASN142:OD1) with the length of 2.3, 2.2, 3.2, 3.2 and 3.07 Å, respectively. The amino acids involved in hydrophobic interaction were shown in Fig. 6 & Table 4.

The number of hydrogen bonds and the distance between ligands and receptors have been demonstrated to be the most essential elements determining the binding affinity of a ligand-receptor interaction in numerous molecular docking studies [53]. As a result, this reason explains why the designed molecule was able to bind tightly to the active pocket of the target enzyme. Overall, the findings of molecular docking interaction analysis revealed that His41, Cys145, and Glu166 amino acid residues were involved in a variety of interactions and bonding, including the formation of hydrogen bonds between selected compounds and the main protease. These amino acids contain the most important part of S1 pocket of main protease. Glu166 mainly responsible for the maintenance of the S1 pocket's shape and stability after forming hydrogen bond and well supported by His41 and Cys145 [39,54].



**Table 6** Drug-likeness prediction data obtained from SwissADME server (MW = Molecular Weight, TPSA = total polar surface area, Consensus Log P = average of all predicted Log Po/w).

Compounds	MW (g/mol)	Rotatable bonds	H-bond acceptors	H-bond donors	TPSA (Å <sup>2</sup> )	Consensus Log P	Lipinski violations	Ghose violations	Veber violations	Egan violations	Muegge violations	Bioavailability Score	Synthetic Accessibility
C6	297.28	2	5	2	71.18	2.72	0	0	0	0	0	0.55	3.41
C7	299.27	2	5	1	50.95	3.44	0	0	0	0	0	0.55	3.44
C8	313.28	2	6	3	91.41	2.35	0	0	0	0	0	0.55	3.52
C10	349.28	3	7	1	50.95	4.17	0	0	0	0	0	0.55	3.57
C11	315.73	2	4	1	50.95	3.66	0	0	0	0	0	0.55	3.41

**Table 7** Showing results of toxicity prediction of selected compounds obtained from pkCSM server.

Compounds	AMES toxicity	Max. tolerated dose (Human)	hERG I inhibitor	hERG II inhibitor	Oral Rat Acute Toxicity (LD50)	Oral Rat Chronic Toxicity (LOAEL)	Hepatotoxicity	Skin sensitisation	T. pyriformis toxicity	Minnow toxicity
<b>C6</b>	Yes	0.269	No	Yes	2.959	1.225	No	No	0.301	0.125
<b>C7</b>	No	0.264	No	Yes	2.964	1.149	No	No	0.302	-0.385
<b>C8</b>	No	0.814	No	Yes	2.945	1.491	No	No	0.289	-0.455
<b>C10</b>	No	0.235	No	Yes	3.035	0.809	Yes	No	0.301	-0.666
<b>C11</b>	No	0.275	No	Yes	2.981	1.094	Yes	No	0.303	-0.718

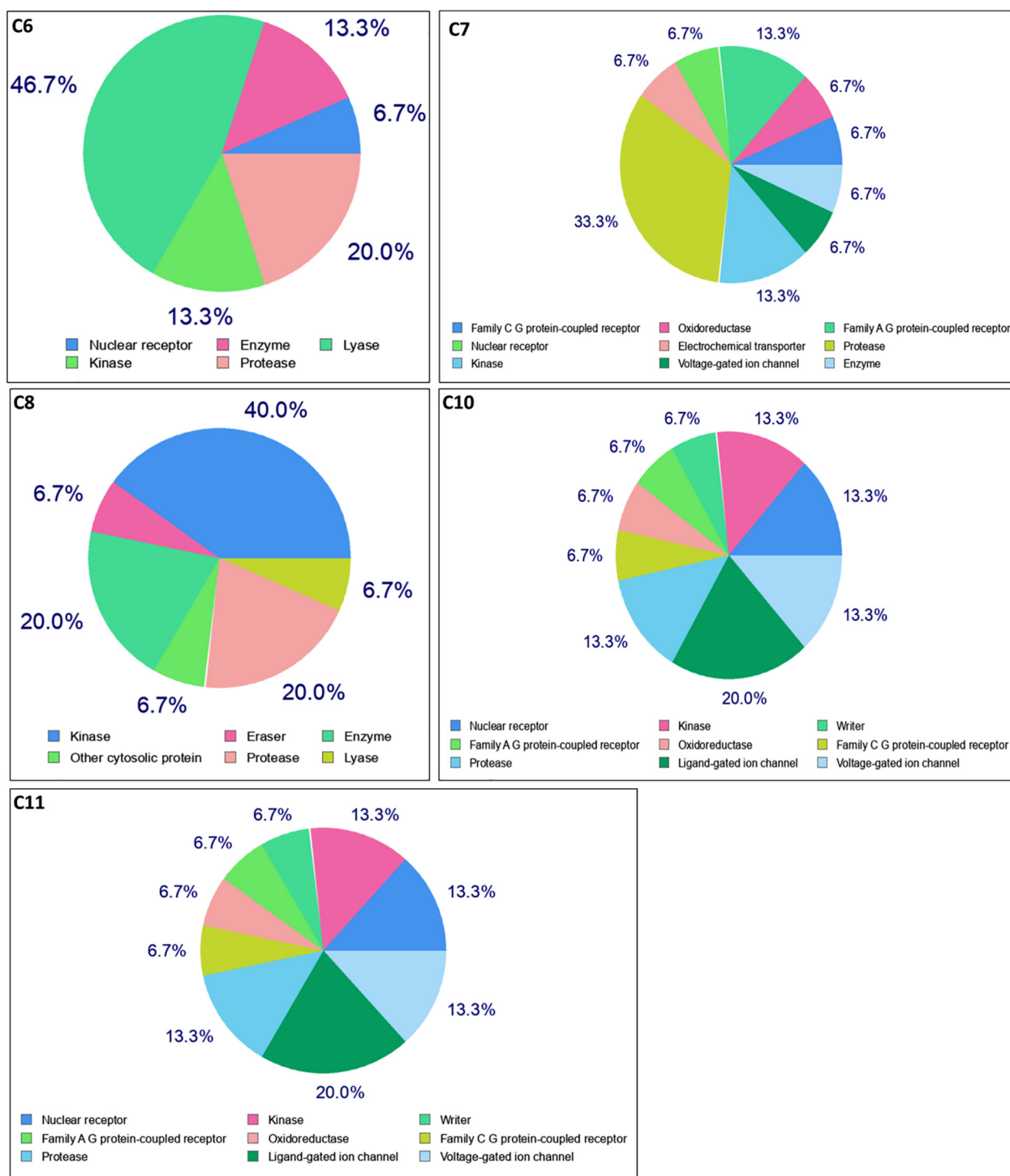


Fig. 8 SwissTargetPrediction of C6, C7, C10 and C11.

### 3.6. ADME, Drug-likeness and toxicity

The antibacterial results encouraged us to undertake ADMET and drug-likeness predictions of the active compounds i.e., A6, A7, A8, A10, and A11. It has been well-known that an inhibitor's antagonistic response to an enzyme or a protein receptor does not guarantee its suitability as a potential drug [20]. Therefore, ADMET, as well as drug-likeness analysis,

are important in drug discovery, as they aid in making a rational decision on whether inhibitors can be administered to biological systems or not. Furthermore, inhibitors with low or poor ADME qualities, as well as severe toxicity effects on biological systems, are frequently the primary reason of failure medicines in clinical trials research.

ADME properties were tested based on several parameters like GI = Gastro intestinal absorption, BBB = Blood Brain

Barrier, Pgp = P glycoprotein, CYP = Cytochrome, log K<sub>p</sub> = skin permeation (Table 5). SwissADME tool was utilized and resulting output suggested that compound A6, A7, A8, A10, and A11 have high GI absorption. Also, generated BOILED-Egg graph (Fig. 7) shown that except A8 all selected compounds were found in yellow part in BOILED-Egg's yolk model which mean A6, A7, A10 and A11 are the compounds predicted to passively permeate through the blood–brain barrier (BBB). Further all compounds have Pgp substrate binding capability. As much as negative the log K<sub>p</sub> value means that the molecule could be less skin permeant, therefore, all selected compounds A6, A7, A8, A10, and A11 have less skin permeability (Table 5).

Drug-likeness prediction provide another way for the analysis of the drug like behavior and physicochemical properties of selected compounds. All the compounds did not show Lipinski violations, Ghose violations, Veber violations and Egan violations. Topological polar surface area (TPSA), has been established as main parameter for the ADME properties assessment of the compounds in context with the BBB crossing TPSA value should be between 20 and 130 Å<sup>2</sup> [57]. Compounds A6, A7, A8, A10, and A11 have TPSA values within the satisfactory range (Table). SwissADME server output also provide a consensus log P<sub>o/w</sub> value, contain the arithmetic mean of Log Po/w (iLOGP), Log Po/w (XLOGP3), Log Po/w (WLOGP), Log Po/w (MLOGP) and Log Po/w (SILICOS-IT) [55,56]. Consensus Log P value should not be higher than 6. Observed values of all selected compounds for this parameter were between 2.35 and 4.17 (Table 6).

pkCSM server toxicity analysis results suggested that compound A7, A8, A10 and A11 not having AMES toxicity except A6, generally AMES toxicity analysis assess the mutagenic capability of chemical compounds. and only A10 and A11 shown hepatotoxicity. *T. pyriformis* toxicity values > 0.5 log ug/L will be considered as toxic properties of the compound. Selected compounds shown values between 0.289 and 0.301. Hence, observed results established compounds A6, A7, A8, A10, and A11 as a non-toxic. Further, no skin sensation was predicted for all compounds. Maximum tolerated dose (Human) should be < = 0.477 log (mg/kg/day). Observed values for human dose parameter were ranged between 0.235 and 0.275 for A6, A7, A10 and A11, while it was higher for A8 with the value 0.814 (Table 7).

### 3.7. SwissTargetPrediction

SwissTargetPrediction is an online tool that predicts the macromolecular targets of bioactive small molecules (proteins from humans, mice, and rats). This is useful for deciphering the molecular pathways underlying a certain phenotypic or bioactivity, rationalizing potential side effects, predicting off-target effects, and evaluating the feasibility of repurposing therapeutically relevant molecules [40]. In the present study, the top 15 targets were selected for the A6, A7, A8, A10, and A11 from output data generated by SwissTarget server. It was found that A6 have 46.7% binding probability to interact with nuclear receptor types of biomolecules whereas A7 shown 33.3% interaction possibilities with protease and A8 have 40% binding capability with kinase while A10 and A11 shows 20% interaction with ligand gated ion channel and 13.3% with kinase, voltage gated ion channel, nuclear recep-

tor, and protease. It was observed that A7 have maximum interaction probability with protease kind of biomolecules (Fig. 8).

## 4. Conclusion

In summary, 17 new Indole-based-oxadiazole compounds were obtained, and were characterized by various techniques. The synthesized compounds showed excellent antibacterial and antibiofilm activity against multi drug resistant gram positive and gram- negative bacteria. The synthesized compounds demonstrated favorable calculated values of interaction energy in the molecular docking with the bacterial peptidoglycan and SARS CoV-2 main protease. The ADME/Tox analysis predicted high GI absorption, BBB permeability and substrate binding affinity with Pgp. The compounds A6, A7, A8, A10, and A11 were predicted to display low toxicity levels. The Consensus Log P values of top ranked compounds were in the range of 2.35 to 4.17 whereas the total polar surface area (TPSA) were in the satisfactory range 50.95 – 91.41 and the bioavailability score was 0.55. Further, each of the tested compounds showed drug-likeness according to the Lipinski, Ghose, Egan, Muegge and Veber rules. Our findings suggest that the synthesized compounds could be promising candidate for the prevention and treatment of biofilm-related microbial infections as well as infection caused by deadly SARS-CoV2.

## Funding

Author Mohammad Azam Ansari would like to thanks to the Deanship of Scientific Research, Imam Abdulrahman Bin Faisal University, Dammam, Saudi Arabia, Grant number-Covid19-2020-002-IRMC.

## Declaration of Competing Interest

The authors declare that they have no known competing financial interests or personal relationships that could have appeared to influence the work reported in this paper.

## Acknowledgements

MAA would like to thanks the Deanship of Scientific Research, Imam Abdulrahman Bin Faisal University, Dammam, Saudi Arabia, for providing Grant number-Covid19-2020-002-IRMC.

## References

- [1] U. Desselberger, Emerging and re-emerging infectious diseases, *J. Infect.* 40 (1) (2000) 3–15.
- [2] M.A. Ansari, H.M. Khan, A.A. Khan, A. Sultan, A. Azam, Synthesis and characterization of the antibacterial potential of ZnO nanoparticles against extended-spectrum β-lactamases-producing *Escherichia coli* and *Klebsiella pneumoniae* isolated from a tertiary care hospital of North India, *Appl. Microbiol. Biotechnol.* 94 (2) (2012) 467–477.
- [3] M.A. Ansari, H.M. Khan, A.A. Khan, S.S. Cameotra, Q. Saquib, J. Musarrat, Gum arabic capped-silver nanoparticles inhibit biofilm formation by multi-drug resistant strains of *Pseudomonas aeruginosa*, *J. Basic Microbiol.* 54 (7) (2014) 688–699.

- [4] <https://www.worldometers.info/coronavirus/>.
- [5] M. Missioui, M.A. Said, G. Demirtaş, J.T. Mague, A. Al-Sulami, N.S. Al-Kaff, Y. Ramli, A possible potential COVID-19 drug candidate: Diethyl 2-(2-(2-(3-methyl-2-oxoquinoxalin-1(2H)-yl) acetyl) hydrazono) malonate: Docking of disordered independent molecules of a novel crystal structure, HSA/DFT/XRD and cytotoxicity, *Arabian J. Chem.* 15 (2) (2022).
- [6] J. Akhtar, A.A. Khan, Z. Ali, R. Haider, M.S. Yar, Structure-activity relationship (SAR) study and design strategies of nitrogen-containing heterocyclic moieties for their anticancer activities, *Eur. J. Med. Chem.* 125 (2017) 143–189.
- [7] F.F. Barsoum, H.M. Hosni, A.S. Girgis, Novel bis (1-acyl-2-pyrazolines) of potential anti-inflammatory and molluscicidal properties, *Bioorg. Med. Chem.* 14 (11) (2006) 3929–3937.
- [8] S. Kumar, S. Bawa, S. Drabu, R. Kumar, H. Gupta, Biological activities of pyrazoline derivatives-A recent development, *Recent Pat. Anti-Infect. Drug Discovery* 4 (3) (2009) 154–163.
- [9] B.P. Bandgar, L.K. Adsul, H.V. Chavan, S.S. Jalde, S.N. Shringare, R. Shaikh, R.J. Meshram, R.N. Gacche, V. Masand, Synthesis, biological evaluation, and docking studies of 3-(substituted)-aryl-5-(9-methyl-3-carbazole)-1H-2-pyrazolines as potent anti-inflammatory and antioxidant agents, *Bioorg. Med. Chem. Lett.* 22 (18) (2012) 5839–5844.
- [10] Sundberg R.J. *Indoles* Academic Press. San Diego. 1996;113.
- [11] P. Singh, Structural optimization of indole based compounds for highly promising anti-cancer activities: Structure activity relationship studies and identification of lead molecules, *Eur. J. Med. Chem.* 74 (2014) 440–450.
- [12] S.K. Sharma, P. Kumar, B. Narasimhan, K. Ramasamy, V. Mani, R.K. Mishra, A.B. Majeed, Synthesis, antimicrobial, anticancer evaluation and QSAR studies of 6-methyl-4-[1-(2-substituted-phenylamino-acetyl)-1H-indol-3-yl]-2-oxo/thioxo-1, 2, 3, 4-tetrahydropyrimidine-5-carboxylic acid ethyl esters, *Eur. J. Med. Chem.* 48 (2012) 16–25.
- [13] S. Mehndiratta, Y.L. Hsieh, Y.M. Liu, A.W. Wang, H.Y. Lee, L.Y. Liang, S. Kumar, C.M. Teng, C.R. Yang, J.P. Liou, Indole-3-ethylsulfamoylphenylacrylamides: potent histone deacetylase inhibitors with anti-inflammatory activity, *Eur. J. Med. Chem.* 85 (2014) 468–479.
- [14] L.P. Liew, J.M. Fleming, A. Longeon, E. Mouray, I. Florent, M.L. Bourguet-Kondracki, B.R. Copp, Synthesis of 1-indolyl substituted  $\beta$ -carboline natural products and discovery of antimalarial and cytotoxic activities, *Tetrahedron* 70 (33) (2014) 4910–4920.
- [15] E. Yamuna, R.A. Kumar, M. Zeller, K.J. Prasad, Synthesis, antimicrobial, antimycobacterial and structure-activity relationship of substituted pyrazolo-, isoxazolo-, pyrimido- and mercaptoprimidocyclohepta [b] indoles, *Eur. J. Med. Chem.* 47 (2012) 228–238.
- [16] T. Noreen, M. Taha, S. Imran, S. Chigurupati, F. Rahim, M. Selvaraj, N.H. Ismail, J.I. Mohammad, H. Ullah, M.T. javid, F. Nawaz, M. Irshad, M. Ali, Synthesis of alpha amylase inhibitors based on privileged indole scaffold, *Bioorg. Chem.* 72 (2017) 248–255.
- [17] O. Abid, S. Imran, M. Taha, N.H. Ismail, W. Jamil, S.M. Kashif, K.M. Khan, J. Yusoff, Synthesis,  $\beta$ -glucuronidase inhibition and molecular docking studies of cyano-substituted bisindole hydrazone hybrids, *Mol. Diversity* 25 (2) (2021) 995–1009.
- [18] M. Taha, F. Rahim, A.A. Khan, E.H. Anouar, N. Ahmed, S.A. Shah, M. Ibrahim, Z.A. Zakari, Synthesis of diindolylmethane (DIM) bearing thiadiazole derivatives as a potent urease inhibitor, *Sci. Rep.* 10 (1) (2020) 1–2.
- [19] J. Lunagariya, P. Bhadja, S. Zhong, R. Vekariya, S. Xu, Marine natural product bis-indole alkaloid caulerpin: Chemistry and biology, *Mini Rev. Med. Chem.* 19 (9) (2019) 751–761.
- [20] R. Filler, R. Saha, Fluorine in medicinal chemistry: a century of progress and a 60-year retrospective of selected highlights, *Future Med. Chem.* 1 (5) (2009) 777–791.
- [21] J. Wang, M. Sánchez-Roselló, J.L. Aceña, C. Del Pozo, A.E. Sorochinsky, S. Fustero, V.A. Soloshonok, H. Liu, Fluorine in pharmaceutical industry: fluorine-containing drugs introduced to the market in the last decade (2001–2011), *Chem. Rev.* 114 (4) (2014) 2432–2506.
- [22] Y. Zhou, J. Wang, Z. Gu, S. Wang, W. Zhu, J.L. Aceña, V.A. Soloshonok, K. Izawa, H. Liu, Next generation of fluorine-containing pharmaceuticals, compounds currently in phase II–III clinical trials of major pharmaceutical companies: new structural trends and therapeutic areas, *Chem. Rev.* 116 (2) (2016) 422–518.
- [23] E.A. Iardi, E. Vitaku, J.T. Njardarson, Data-mining for sulfur and fluorine: An evaluation of pharmaceuticals to reveal opportunities for drug design and discovery: Miniperspective, *J. Med. Chem.* 57 (7) (2014) 2832–2842.
- [24] S.N. Bukhari, X. Zhang, I. Jantan, H.L. Zhu, M.W. Amjad, V. H. Masand, Synthesis, molecular modeling, and biological evaluation of novel 1, 3-diphenyl-2-propen-1-one based pyrazolines as anti-inflammatory agents, *Chem. Biol. Drug Des.* 85 (6) (2015) 729–742.
- [25] C.-H. Zhou, Y. Wang, Recent researches in triazole compounds as medicinal drugs, *Curr. Med. Chem.* 19 (2) (2012) 239–280.
- [26] M.A. Ansari, S. Akhtar, M.A. Rauf, M.N. Alomary, S. AlYahya, S. Alghamdi, M.A. Almessiere, A. Baykal, F. Khan, S.F. Adil, M. Khan, Sol-Gel synthesis of Dy-substituted Ni<sub>0.4</sub>Cu<sub>0.2</sub>Zn<sub>0.4</sub>(Fe<sub>2-x</sub>Dy<sub>x</sub>)O<sub>4</sub> nano spinel ferrites and evaluation of their antibacterial, antifungal, antibiofilm and anticancer potentialities for biomedical application, *Internat. J. Nanomed.* 16 (2021), 5633.
- [27] D.S. Wishart, C. Knox, A.C. Guo, D. Cheng, S. Shrivastava, D. Tzur, B. Gautam, M. Hassanali, DrugBank: a knowledgebase for drugs, drug actions and drug targets, *Nucleic Acids Res.* 36 (suppl\_1) (2008) D901–D906.
- [28] BIOVIA, Dassault Systèmes, [Discovery Studio visualizer], [2020], San Diego: Dassault Systèmes, [2020].
- [29] H.M. Berman, J. Westbrook, Z. Feng, G. Gilliland, T.N. Bhat, H. Weissig, I.N. Shindyalov, P.E. Bourne, The protein data bank, *Nucleic Acids Res.* 28 (1) (2000) 235–242.
- [30] L.K. Wolf, New software and websites for the chemical enterprise, *Chem. Eng. News Archive.* 87 (2009) 31.
- [31] O. Trott, A.J. Olson, AutoDock Vina: improving the speed and accuracy of docking with a new scoring function, efficient optimization and multithreading, *J. Comput. Chem.* 31 (2010) 455–461.
- [32] A.M. Elsharif, T.E. Youssef, S.S. Al-Jameel, H.H. Mohamed, M.A. Ansari, S. Rehman, S. Akhtar, Synthesis of an activatable tetra-substituted nickel phthalocyanines-4 (3H)-quinazolinone conjugate and its antibacterial activity, *Adv. Pharmacol. Sci.* 2019 (2019) 1–10.
- [33] U. Baig, M.A. Gondal, M.A. Dastageer, M.A. Ansari, M. Sajid, W.S. Falath, Synthesis of cadmium sulfide-tungsten trioxide nanocomposites for photo-catalytic degradation of organic pollutants and growth retardation of waterborne bacteria and biofilms, *Colloids Surf., A* 606 (2020) 125423.
- [34] K. Vanommeslaeghe, E. Hatcher, C. Acharya, S. Kundu, S. Zhong, J. Shim, E. Darian, O. Guvench, P. Lopes, I. Vorobyov, A.D. Mackerell Jr, CHARMM general force field: A force field for drug-like molecules compatible with the CHARMM all-atom additive biological force fields, *J. Comput. Chem.* 31 (4) (2010) 671–690.
- [35] M.A. Ansari, S.M.M. Asiri, Green synthesis, antimicrobial, antibiofilm and antitumor activities of superparamagnetic  $\gamma$ -Fe<sub>2</sub>O<sub>3</sub> NPs and their molecular docking study with cell wall mannoproteins and peptidoglycan, *Int. J. Biol. Macromol.* 171 (2021) 44–58.
- [36] Z. Jin, X. Du, Y. Xu, Y. Deng, M. Liu, Y. Zhao, B. Zhang, X. Li, L. Zhang, C. Peng, Y. Duan, J. Yu, L. Wang, K. Yang, F. Liu, R. Jiang, X. Yang, T. You, X. Liu, X. Yang, F. Bai, H. Liu,

- X. Liu, L.W. Guddat, W. Xu, G. Xiao, C. Qin, Z. Shi, H. Jiang, Z. Rao, H. Yang, Structure of M pro from SARS-CoV-2 and discovery of its inhibitors, *Nature* 582 (7811) (2020) 289–293.
- [37] M. Rudrapal, I. Celik, J. Khan, M.A. Ansari, M.N. Alomary, F. A. Alatawi, R. Yadav, T. Sharma, T.E. Tallei, P.K. Pasala, R.K. Sahoo, S.J. Khairnar, A.R. Bendale, J.H. Zothantluanga, D. Chetia, S.G. Walode, Identification of bioactive molecules from Triphala (Ayurvedic herbal formulation) as potential inhibitors of SARS-CoV-2 main protease (Mpro) through computational investigations, *J. King Saud Univ.-Sci.* 34 (3) (2022).
- [38] S. Dallakyan, A.J. Olson, Small-molecule library screening by docking with PyRx, in: *InChemical Biology*, Humana Press, New York, NY, 2015, pp. 243–250.
- [39] L. Zhang, D. Lin, X. Sun, U. Curth, C. Drosten, L. Sauerhering, S. Becker, K. Rox, R. Hilgenfeld, Crystal structure of SARS-CoV-2 main protease provides a basis for design of improved  $\alpha$ -ketoamide inhibitors, *Science* 368 (6489) (2020) 409–412.
- [40] A. Daina, O. Michielin, V. Zoete, SwissADME: a free web tool to evaluate pharmacokinetics, drug-likeness and medicinal chemistry friendliness of small molecules, *Sci. Rep.* 7 (2017) 42717.
- [41] Q.M.S. Jamal, M.U. Siddiqui, A.H. Alharbi, F. Albejaidi, S. Akhtar, M.A. Alzohairy, M.A. Kamal, K.K. Kesari, A computational study of natural compounds from *Bacopa monnieri* in the treatment of Alzheimer's disease, *Curr. Pharm. Des.* 26 (7) (2020) 790–800.
- [42] D.E. Pires, T.L. Blundell, D.B. Ascher, pkCSM: predicting small-molecule pharmacokinetic and toxicity properties using graph-based signatures, *J. Med. Chem.* 58 (9) (2015) 4066–4072.
- [43] D. Gfeller, A. Grosdidier, M. Wirth, A. Daina, O. Michielin, V. Zoete, SwissTargetPrediction: a web server for target prediction of bioactive small molecules, *Nucleic Acids Res.* 42 (Web Server issue) (2014) W32–8.
- [44] N.K. Zawawi, M. Taha, N. Ahmat, A. Wadood, N.H. Ismail, F. Rahim, M. Ali, N. Abdullah, K.M. Khan, Novel 2, 5-disubstituted-1, 3, 4-oxadiazoles with benzimidazole backbone: A new class of  $\beta$ -glucuronidase inhibitors and in silico studies, *Bioorg. Med. Chem.* 23 (2015) 3119–3125.
- [45] H. Shirinzadeh, N. Altanlar, N. Yucel, S. Ozden, S. Suzen, Antimicrobial evaluation of indole-containing hydrazone derivatives, *Zeitschrift für Naturforschung C.* 66 (7–8) (2011) 340–344.
- [46] M.Z. Zhang, N. Mulholland, D. Beattie, D. Irwin, Y.C. Gu, Q. Chen, G.F. Yang, J. Clough, Synthesis and antifungal activity of 3-(1, 3, 4-oxadiazol-5-yl)-indoles and 3-(1, 3, 4-oxadiazol-5-yl) methyl-indoles, *Eur. J. Med. Chem.* 63 (2013) 22–32.
- [47] H. Kandemir, C. Ma, S.K. Kuty, D.S. Black, R. Griffith, P.J. Lewis, N. Kumar, Synthesis and biological evaluation of 2, 5-di (7-indolyl)-1, 3, 4-oxadiazoles, and 2-and 7-indolyl 2-(1, 3, 4-thiadiazolyl) ketones as antimicrobials, *Bioorg. Med. Chem.* 22 (5) (2014) 1672–1679.
- [48] K. Biernacki, M. Daško, O. Ciupak, K. Kubiński, J. Rachon, S. Demkowicz, Novel 1, 2, 4-oxadiazole derivatives in drug discovery, *Pharmaceuticals* 13 (6) (2020) 111.
- [49] X. Yao, M. Jericho, D. Pink, T. Beveridge, Thickness and elasticity of gram-negative murein sacculi measured by atomic force microscopy, *J. Bacteriol.* 181 (22) (1999) 6865–6875.
- [50] S. Bala, S. Kamboj, A. Kajal, V. Saini, D.N. Prasad, 1,3,4-Oxadiazole derivatives: synthesis, characterization, antimicrobial potential, and computational studies, *Biomed Res. Int.* 2014 (2014) 1–18.
- [51] Y. Zheng, L. He, T.K. Asiamah, M. Otto, Colonization of medical devices by staphylococci, *Environ. Microbiol.* 20 (9) (2018) 3141–3153.
- [52] L. Yamani, A. Alamri, A. Alsultan, S. Alfifi, M.A. Ansari, A. Alnimir, Inverse correlation between biofilm production efficiency and antimicrobial resistance in clinical isolates of *Pseudomonas aeruginosa*, *Microb. Pathog.* 157 (2021).
- [53] S. Elijah, A. David, E. Arthur, M. Abdullahi, A. Haruna, Quantitative structure–activity relationship model, molecular docking simulation and computational design of some novel compounds against DNA gyrase receptor, *Chem Afr.* 3 (2020) 391–408.
- [54] Q.M. Sajid Jamal, A.H. Alharbi, V. Ahmad, Identification of doxorubicin as a potential therapeutic against SARS-CoV-2 (COVID-19) protease: a molecular docking and dynamics simulation studies, *J. Biomol. Struct. Dyn.* 23 (2021) 1–5.
- [55] A. Daina, V. Zoete, A boiled-egg to predict gastrointestinal absorption and brain penetration of small molecules, *ChemMedChem* 11 (11) (2016) 1117–1121.
- [56] M.S. Malik, S.F. Adil, Z.S. Seddigi, M. Morad, R.S. Jassas, I.I. Thagafi, H.M. Altass, Q.M. Sajid Jamal, S. Riyaz, R.I. Alsantali, A.A. Al-Warthan, M.A. Ansari, S.A. Ahmed, Molecular modelling assisted design of naphthalimide-dihydropyrimidinone conjugates as potential cytotoxic agents, *J. Saudi Chem. Soc.* 25 (5) (2021).
- [57] P. Ertl, B. Rohde, P. Selzer, Fast calculation of molecular polar surface area as a sum of fragment-based contributions and its application to the prediction of drug transport properties, *J. Med. Chem.* 43 (20) (2000) 3714–3717.